MATHEMATICAL MODELING IN HEALTH AND DISEASE

By

JESSICA A. BRADY

(Under the Direction of K. Melissa Hallow and Juan B. Gutierrez)

ABSTRACT

Mathematical modeling is the process of quantitatively describing a particular system, process, or phenomenon. It can be utilized to detect patterns and interactions that cannot be understood with the current data available and to test hypotheses that are difficult to evaluate experimentally. In this dissertation, mathematical modeling is used in three unique ways. (1) We extended an existing mathematical model of glucose and insulin dynamics to account for renal filtration and excretion of glucose, in order to investigate the effect of treatment for a diabetes medication. We quantified and compared daily glucose and sodium reabsorption through sodium glucose cotransporters 2 (SGLT2) in healthy, controlled, and uncontrolled diabetes and following treatment with an SGLT2 inhibitor. (2) We captured high frequency physiological data (e.g. temperature, blood pressure) via telemetry from nonhuman primates during health and malaria infection. Using a multiple-component cosinor model, we were able to quantify changes

in biological rhythm parameters that helped classify between health and disease states. (3) We created a model of erythrocytic glucose to investigate the role of malaria parasite glucose utilization on red blood cell bursting cycles. The malaria parasite cannot store energy and relies on the host's erythrocytic glucose. Infected erythrocytes burst at regular 24, 48, or 72 hr intervals. The model was applied to understand and propose experimentally testable hypotheses regarding the role of malaria parasites in altering cell energy availability and triggering bursting. Overall, mathematical modeling in these research areas provided novel insights into the various health and disease states.

INDEX WORDS: Mathematical Modeling, Diabetes, Malaria, Telemetry, Quantitative Systems Pharmacology

MATHEMATICAL MODELING IN HEALTH AND DISEASE

By

JESSICA A. BRADY

B.S., John Brown University, 2013

A Dissertation Submitted to the Graduate Faculty of The University of Georgia in Partial Fulfillment of the Requirements for the Degree

DOCTOR OF PHILOSOPHY

ATHENS, GEORGIA

2019

© 2019

Jessica A. Brady

All Rights Reserved

MATHEMATICAL MODELING IN HEALTH AND DISEASE

by

JESSICA A. BRADY

Major Professor:	K. Melissa Hallow
	Juan B. Gutierrez
Committee:	Caner Kazanci
	Xianqiao Wang
	Jonathan Arnold

Electronic Version Approved:

Suzanne Barbour
Dean of the Graduate School
The University of Georgia
August 2019

DEDICATION

To my family

ACKNOWLEDGEMENTS

I would like to thank my advisors, committee members, instructors, colleagues, friends, and family who have supported me and helped make this work possible. I would sincerely like to express my appreciation for my advisors Dr. Melissa Hallow and Dr. Juan B. Gutierrez for their invaluable direction and support throughout my Ph.D. work. I am indebted to them for their patience, instruction, scholarship, encouragement, and time spent helping me develop my written and oral communication skills, critical thinking, and scientific curiosity. I would also like to thank Dr. Caner Kazanci, Dr. Xianqiao Wang, and Dr. Jonathan Arnold for serving as members on my committee and for their scientific insight.

I would like to acknowledge my family and friends for their love, encouragement, and support which have given me strength to persevere. Finally, I would like to thank Quentin Brady, my husband, my best friend, my love, and my greatest supporter.

TABLE OF CONTENTS

LIST OF TABLES

Page

LIST OF FIGURES

Page

CHAPTER 1

INTRODUCTION

1.1 BACKGROUND AND MOTIVATION

Mathematical modeling is the process of quantitatively describing a particular system, process, or phenomenon. It can be utilized to detect patterns and interactions that cannot be understood with the current data available and to test hypotheses that are difficult to evaluate experimentally. Mathematical models describing populations and the transmission of infectious diseases have been successful in epidemiology allowing public health officials to predict where an outbreak could be eminent or where a past outbreak may have started. In addition to the scale of human populations, mathematical modeling can also be used to quantify a process that is not visible to the eye, such as action potential in a neuron[1]. Mathematical modeling is used in a variety of scales and disease contexts in this dissertation.

1.1.1 Diabetes Medication

Sodium-glucose cotransporter 2 inhibitors (SGLT2i) reduce glucose levels in diabetes by inhibiting renal glucose reabsorption in the proximal tubule, resulting in urinary glucose excretion. A recent large cardiovascular outcomes trial[2] suggested that the SGLT2i empagliflozin may also decrease risk of renal dysfunction. Because sodium (Na) and glucose reabsorption are coupled through SGLT2, it is hypothesized that the renal benefits may be derived from lowering Na reabsorption in the PT, which would lead to favorable renal hemodynamic changes.

However, the quantitative contribution of SGLT2 to PT Na reabsorption, as well as the differences between healthy and diabetic subjects, and the impact of SGLT2i on PT Na reabsorption are unknown.

1.1.2 Telemetry and Disease Detection for Malaria

Early detection of physiological changes due to infectious diseases, such as malaria, could guide treatment prior to the onset of symptoms and pathogenic consequences. Current malaria diagnostic tests, generally used once a patient has symptoms, confirm the presence of infections caused by malaria parasites in the blood. However, when the host initially gets infected, the malaria parasite travels to the liver and is undetectable in the blood for a period of days. A diagnostic method is needed that would detect the parasite's presence during this liver stage period preceding blood-stage infections and symptomology. Early treatment may reduce the prospects for complications[3,4,5], and can lead to a decrease in transmission of the infectious disease, thus protecting others in the community.

1.1.3 Malaria Parasite and Glucose Interactions

The malaria parasite cannot store energy and instead relies on host erythrocytic glucose as an energy source during the human blood stage. The exact mechanism for synchronization of the erythrocytic cycle bursting is unknown. Traditionally, this synchronization of erythrocyte bursting was thought to be related to light stimulus. A recent published study[6] showed that the erythrocytic cycle timing changes 12 hours based on nightly feeding times as opposed to daily feeding times; this suggests that glucose availability could be related to this synchronization. A better understanding of the interaction between the host's erythrocytes glucose concentrations

and the malaria parasite is needed to aid in the development of future treatment strategies to combat disease progression.

1.2 OBJECTIVE, HYPOTHESIS, AND SPECIFIC AIMS

The proposed research aims propose to use mathematical modeling to provide novel insights into the various health and disease contexts.

1.2.1 Specific Aim 1: Extend an existing mathematical model of glucose and insulin dynamics to quantify renal filtration, reabsorption, and excretion of glucose and sodium in healthy, controlled, and uncontrolled diabetes and following treatment with canagliflozin, an SGLT2i.

The objective of this aim was to build a model that could quantify daily proximal tubule reabsorption through sodium glucose cotransporter 2 (SGLT2) under normal and diabetic conditions and following treatment with an SGLT2 inhibitor. Since sodium and glucose reabsorption are coupled through SGLT2, it is **hypothesized** that lowering sodium reabsorption in the proximal tubule may lead to favorable renal hemodynamic changes. Once the published model[7-9] was extended, model fitting with published data was conducted to identify parameters representing both healthy and type 2 diabetes mellitus (T2DM) subjects. The renal threshold for glucose parameter was specifically estimated (with all other parameters fixed) for different SGLT2i doses using published data in order to model the pharmacologic effects of an SGLT2i. Model simulations were then performed using these parameter sets to quantify (1) the contribution of SGLT2 to PT sodium reabsorption under normal conditions, (2) the degree to

which PT sodium reabsorption through SGLT2 is increased in diabetes, and (3) the reduction in PT sodium reabsorption due to SGLT2 inhibition.

1.2.2 Specific Aim 2: Develop and implement a telemetry system, data infrastructure, and analysis pipeline for early detection of physiological changes due to pathogenesis, a case study of malaria.

Our second aim was to quantify biological rhythms in physiological signals (temperature, activity, blood pressure and electrocardiogram) between baseline and infection stages for the malaria parasite, *Plasmodium knowlesi*. We **hypothesize** that there is a disruption in these rhythms due to infection before symptoms occur. We developed telemetry methods to detect and monitor physiological changes in nonhuman primates prior to and in the course of disease progression. Daily biological rhythm parameters were obtained using a multiple-component cosinor model to classify between healthy baseline and infection using machine learning algorithms.

1.2.3 Specific Aim 3: Model the malaria parasite's effect and dependence upon host erythrocytic glucose concentrations.

The objective of this aim was to build a model that quantified glucose and adenosine triphosphate (ATP) concentrations in the red blood cell under healthy conditions and during malaria infection. In order to characterize the interaction between the malaria parasite and erythrocytic glucose concentrations, we needed to describe glucose transport[10] between the plasma and red blood cell and how glucose gets utilized under healthy red blood cell conditions before we could explore the parasite effect. We **hypothesize** that erythrocytic bursting and parasite release could be related to exhaustion of glucose and consequently depleted erythrocytic

ATP levels. By modeling diurnal glucose concentrations and incorporating parasite dynamics, we aim to test our hypothesis mathematically and further investigate the relationship between erythrocytic glucose and parasite synchronization.

1.3 REFERENCES

1. Hodgkin AL, Huxley AF. A quantitative description of membrane current and its application to conduction and excitation in nerve. *The Journal of physiology.* 1952;117(4):500-544.
2. Wanner C, Inzucchi SE, Lachin JM, et al. Empagliflozin and Progression of Kidney Disease in Type 2 Diabetes. *New England Journal of Medicine.* 2016;375(4):323-334.
3. Yang S, Rothman RE. PCR-based diagnostics for infectious diseases: uses, limitations, and future applications in acute-care settings. *The Lancet Infectious Diseases.* 2004;4(6):337-348.
4. Veldhuijzen IK, Toy M, Hahné SJM, et al. Screening and Early Treatment of Migrants for Chronic Hepatitis B Virus Infection Is Cost-Effective. *Gastroenterology.* 2010;138(2):522-530.
5. Gao L, Liu X, Zhang D, et al. Early diagnosis of bacterial infection in patients with septicopyemia by laboratory analysis of PCT, CRP and IL-6. *Experimental and therapeutic medicine.* 2017;13(6):3479-3483.
6. Prior KF, Veen DRvd, O'Donnell AJ, et al. Timing of host feeding drives rhythms in parasite replication. *PLoS Pathogens.* 2018;14(2):e1006900-e1006900.
7. Jauslin PM, Frey N, Karlsson MO. Modeling of 24-Hour Glucose and Insulin Profiles of Patients With Type 2 Diabetes. *The Journal of Clinical Pharmacology.* 2011;51(2):153-164.
8. Jauslin PM, Silber HE, Frey N, et al. An integrated glucose-insulin model to describe oral glucose tolerance test data in type 2 diabetics. *Journal of Clinical Pharmacology.* 2007(10):1244.
9. Silber HE, Jauslin PM, Frey N, Gieschke R, Simonsson USH, Karlsson MO. An Integrated Model for Glucose and Insulin Regulation in Healthy Volunteers and Type 2 Diabetic Patients Following Intravenous Glucose Provocations. *The Journal of Clinical Pharmacology.* 2007;47(9):1159-1171.
10. Alonso GL, González DA. In Silico Kinetic Study of the Glucose Transporter. *Journal of Biological Physics.* 2007;33(5-6):485.

CHAPTER 2

MODEL-BASED EVALUATION OF PROXIMAL SODIUM REABSORPTION THROUGH SGLT2 IN HEALTH AND DIABETES AND THE EFFECT OF INHIBITION WITH CANAGLIFLOZIN[1]

---

[1]Jessica A. Brady and K. Melissa Hallow. Accepted by *The Journal of Clinical Pharmacology*, September 16, 2017. Reprinted here with permission of publisher.

2.1 ABSTRACT

Sodium-glucose cotransporter 2 inhibitors (SGLT2i) reduce glucose levels in diabetes by inhibiting renal glucose reabsorption in the proximal tubule (PT), resulting in urinary glucose excretion. A recent large cardiovascular outcomes trial suggested that the SGLT2i empagliflozin may also decrease risk of renal dysfunction. Because sodium (Na) and glucose reabsorption are coupled through SGLT2, it is hypothesized that the renal benefits may be derived from lowering Na reabsorption in the PT, which would lead to favorable renal hemodynamic changes. However, the quantitative contribution of SGLT2 to PT Na reabsorption, as well as the differences between healthy and diabetic subjects, and the impact of SGLT2i on PT Na reabsorption are unknown. In this study we extended an existing mathematical model of glucose dynamics to account for renal glucose filtration and excretion. We utilized this model to quantify glucose and Na reabsorption through SGLT2 in healthy, controlled, and uncontrolled diabetes and following treatment with canagliflozin. In healthy, controlled diabetic, and uncontrolled diabetic states, Na reabsorption through SGLT2 was found to be 5.7%, 11.5%, and 13.7% of total renal Na reabsorption, and 7.1% to 9.5%, 14.4% to 19.2%, and 17.1% to 22.8% of Na reabsorption in the PT alone. The model predicted that treatment of controlled diabetes with canagliflozin returns PT Na reabsorption through SGLT2 to normal levels. The degree of increased PT Na reabsorption due to SGLT2 is likely sufficient to drive pathologic changes in renal hemodynamics, and restoration of normal Na reabsorption through SGLT2 may contribute to beneficial renal effects of SGLT2 inhibition.

2.2 INTRODUCTION

Diabetes is the leading cause of chronic kidney disease. The progressive decline in glomerular filtration rate (GFR) in diabetic kidney disease is often preceded by a period of hyperfiltration, and the degree of early hyperfiltration is predictive of the subsequent rate of GFR decline.[1] Although the causes of hyperfiltration are still debated, the tubulocentric hypothesis postulates that hyperfiltration is a consequence of a primary increase in proximal tubule (PT) sodium reabsorption in diabetes.[2] We have recently demonstrated this tubular hypothesis of hyperfiltration mathematically and shown that it can produce glomerular hypertension and potentially contribute to renal injury and GFR decline, particularly when coupled with impairment of the pressure-natriuresis mechanism.[3]

The primary increase in PT sodium reabsorption consistently observed in diabetes [4-6] is at least partially due to coupled glucose and sodium reabsorption through sodium glucose cotransporters (SGLT). Under normal conditions nearly all filtered glucose is reabsorbed in the PT, and 90% to 97% of this reabsorption occurs through SGLT2 in the S1 and S2 segments. The remaining 3% to 10% occurs through SGLT1 in the S3 segment of the PT. The capacity for glucose reabsorption through SGLT is not unlimited, and there is a threshold above which excess filtered glucose is excreted in the urine.

SGLT2 inhibitors (SGLT2i) reduce glucose levels in type 2 diabetes mellitus (T2DM) by inhibiting glucose reabsorption in the PT of the kidney, resulting in urinary glucose excretion (UGE). In a recent large clinical trial,[7] the SGLT2 inhibitor empagliflozin was found to dramatically slow the rate of GFR decline in patients with T2DM and decrease cardiovascular risk. Because sodium and glucose reabsorption are coupled through SGLT2, it is hypothesized

that lowering sodium reabsorption in the PT may lead to favorable renal hemodynamic changes and subsequently contribute to renal and cardiovascular protection.

However, the quantitative contribution of SGLT2 to tubular sodium reabsorption, as well as the differences between healthy and diabetic subjects, and the impact of SGLT2i on sodium reabsorption, have not been quantified. In this study we extended an existing mathematical model of glucose and insulin dynamics[8,9] to account for renal filtration and excretion of glucose. We then used this model to quantify daily PT sodium reabsorption through SGLT2 under normal and diabetic conditions and following treatment with an SGLT2 inhibitor.

2.3 METHODS

2.3.1 Model Description

In order to quantify sodium reabsorption through SGLT2, we must first quantify glucose reabsorption because glucose is the rate-limiting factor, and sodium is reabsorbed along with glucose through SGLT2 at a 1:1 molar ratio. To this end, a published mathematical model of glucose and insulin dynamics[8-10] was extended to include renal filtration, reabsorption, and excretion of glucose and sodium, as described below.

Renal Filtration, Reabsorption, and Excretion of Glucose and Sodium. Glucose is filtered freely through the glomerulus so that the filtered glucose load $\Phi_{glu,filtered}$ is a function of the glomerular filtration rate (GFR) and plasma glucose concentration (C_{glu}):

$$\Phi_{glu,filtered} = GFR * C_{glu} \quad \text{(Eq. 2.1)}$$

Under normal conditions filtered glucose is nearly completely reabsorbed through SGLT in the PT, and urinary glucose excretion contributes little to glucose elimination. However, at high plasma concentrations, filtered glucose can exceed the kidney's capacity for reabsorption. The plasma concentration at which filtered glucose exceeds the renal capacity for glucose reabsorption has been defined as the renal threshold for glucose excretion (RT_G).[11]

The renal capacity for glucose reabsorption (RC) is then given by:

$$RC = RT_G * GFR \quad \text{(Eq. 2.2)}$$

The rate of glucose reabsorption in the proximal tubule is then:

$$\Phi_{glu,reabs} = \min(\Phi_{glu,filtered}, RC) \quad \text{(Eq. 2.3)}$$

Any glucose not reabsorbed is then excreted, so that the rate of urinary glucose excretion (RUGE) is:

$$RUGE = \Phi_{glu,filtered} - \Phi_{glu,reabs} \quad \text{(Eq. 2.4)}$$

Thus, when plasma glucose concentration (C_{glu}) is less than the renal threshold for glucose excretion (RT_G), all glucose is reabsorbed, and $\Phi_{glu,excr}$ is 0.When C_{glu} exceeds RT_G, the excess filtered glucose is excreted.

Cumulative glucose reabsorption and cumulative urinary glucose excretion (UGE) are given by:

$$\frac{d(cumGluReabs)}{dt} = \Phi_{glu,reabs} \quad \text{(Eq. 2.5)}$$

$$\frac{d(UGE)}{dt} = RUGE \quad \text{(Eq. 2.6)}$$

Because SGLT2 transports glucose and sodium at a 1:1 molar ratio, the cumulative sodium reabsorbed through SGLT2 is equivalent to glucose reabsorbed through SGLT2:

$$cumNaReabs_{SGLT2} = cumGlucReabs_{SGLT2} \quad \text{(Eq. 2.7)}$$

SGLT2 is only 1 of several transporters involved in sodium reabsorption in the proximal tubule. Cumulatively, all of these transporters reabsorb around 60% to 80% of the filtered sodium load. As with glucose, sodium is freely filtered across the glomerulus, so that filtered sodium load is given by:

$$\Phi_{\text{Na,filtered}} = GFR * C_{Na} \quad \text{(Eq. 2.8)}$$

where C_{Na} is the plasma concentration of Na. Thus, assuming 70% fractional reabsorption, total PT sodium reabsorbed in the PT each day is given by:

$$cumNaReabs_{total} = 0.7 * \Phi_{\text{Na,filtered}} * 24 * 60 \quad \text{(Eq. 2.9)}$$

2.3.2 Glucose and Insulin Model

A previously published model of glucose-insulin dynamics[8-10] was altered to include renal excretion of glucose. The model schematic, adapted from Jauslin et al[9] to show glucose elimination through renal excretion, is shown in Figure 2.1. For full details, the reader is referred to Jauslin and colleagues.[8-10]

In this model the rate of change of glucose in the central (plasma) compartment (GLU_C) is modeled as the sum of glucose absorption rate (ABSG), endogenous glucose production rate (G_{PRO}), glucose elimination rate (G_{ELI}), and glucose distribution rate (G_{DIS}). We have added a term to account for the rate of urinary glucose excretion (RUGE) (Eq. 2.10). Thus, under conditions in which plasma glucose concentration is below the renal threshold for glucose excretion RT_G, the model is identical to the previously published model. But the updated model can now accommodate the case of glucose levels elevated above RT_G, or when RT_G is lowered through SGLT2 inhibition.

$$\frac{d(GLU_C)}{dt} = ABSG + G_{PRO} - G_{ELI} - G_{DIS} - RUGE \quad \text{(Eq. 2.10)}$$

Plasma glucose concentration C_{glu} is given in equation 2.11, where V_G is the central volume of distribution of glucose.

$$C_{glu} = \frac{GLU_C}{V_G} \quad \text{(Eq. 2.11)}$$

All other model equations were taken directly from Jauslin and colleagues.[8-10]

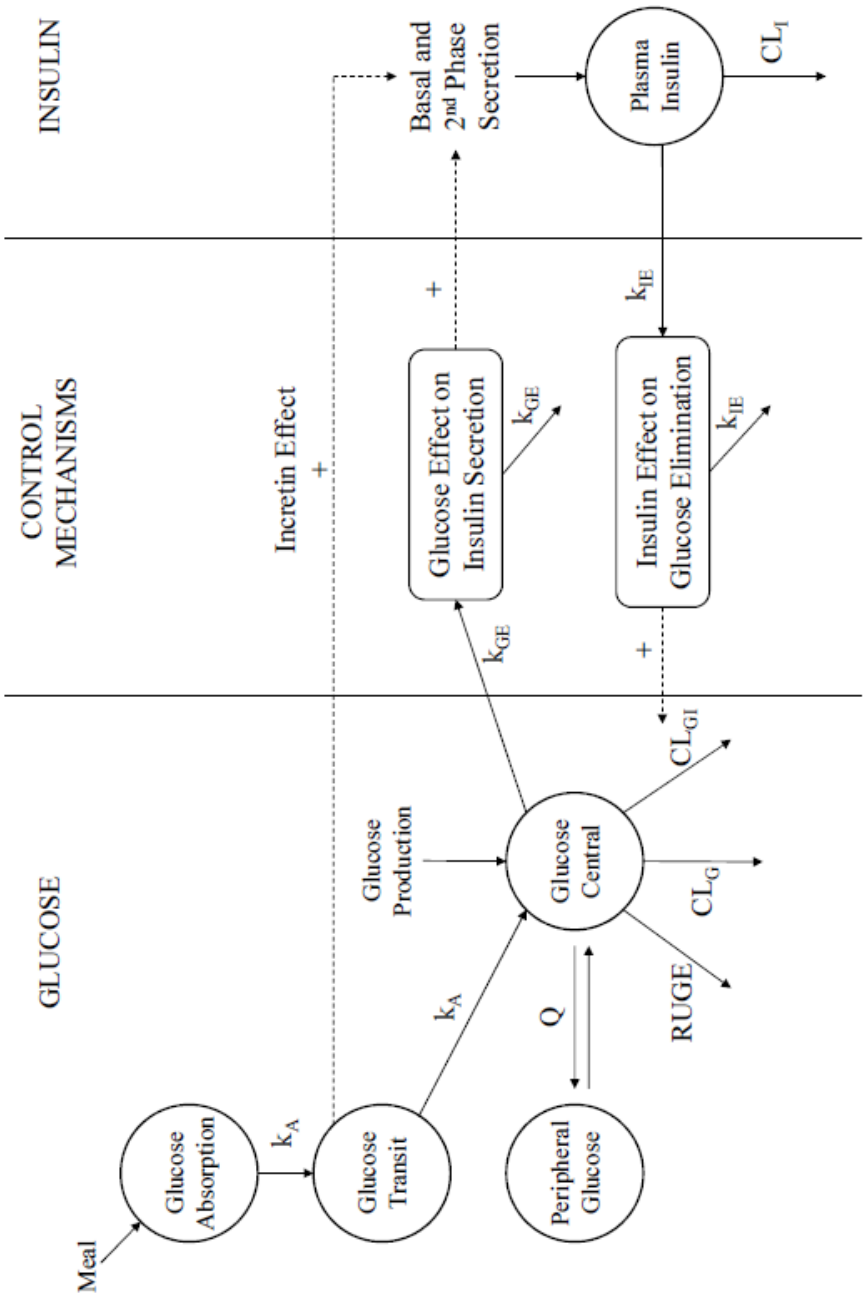

Figure 2.1. Model schematic, adapted from Figure 1 of Jauslin et al.[9] CL_G indicates clearance of glucose; CL_{GI}, insulin-independent glucose clearance; CL_I, clearance of insulin; k_A, rate constant for glucose absorption; k_{GE}, rate constant for glucose-stimulated insulin secretion; k_{IE}, rate constant for insulin effect compartments; Q, equilibrium constant between peripheral and central glucose; RUGE, rate of urinary glucose excretion.

2.3.3 Data

Data were obtained by digitization from a published study in 29 T2DM patients treated with placebo or 50, 100, and 300 mg canagliflozin.[12] In this study patients were required to be on a stable antihyperglycemic regimen with fasting plasma glucose between 140 and 270 mg/dL and HbA_{1c} between 6.5% and 9.5% at baseline. Patients were given 3 standard meals containing approximately 100 g carbohydrates at 10 minutes, 4.5 hours, and 10 hours after administration of the study drug. Plasma glucose was measured with frequent blood samples over 24 hours, and cumulative 24-hour UGE was assessed through urine collection at day –1 and day 1. For full protocol details, see Devineni et al.[12]

2.3.4 Model Fitting

Jauslin et al have used this model previously to describe both healthy subjects[10] and T2DM patients.[8,9] We have updated the model to include the effect of glucose clearance through renal mechanisms. Because healthy subjects experience minimal UGE, the previously estimated parameters describing healthy subjects are still appropriate for simulating healthy subjects.[8,10] However, T2DM subjects may have nonzero UGE at baseline. In addition, there may be substantial variation between diabetic patients in different studies with different inclusion/exclusion criteria. Thus, it was necessary to reestimate a subset of model parameters to describe the T2DM population in Devineni et al.[12] Specifically, we reestimated parameters describing glucose-dependent insulin clearance, the rate of insulin effectiveness, the incretin effect on insulin excretion (S_{inc}), and the newly introduced parameter describing RT_G by simultaneously fitting plasma glucose and 24-hour UGE data from the placebo arm of this study.[12]

Estimation of the Pharmacologic Effects of the SGLT2 Inhibitor Canagliflozin on RT_G. SGLT2 inhibitors like canagliflozin act by effectively reducing the renal threshold for glucose reabsorption.[11] In order to explore the effects of SGLT2 inhibition on glucose and sodium excretion, we first estimated the effect of treatment with canagliflozin on RT_G. For this estimation all other model parameters remained fixed, and RT_G was estimated for each dose of canagliflozin in the study by simultaneously fitting both plasma glucose and UGE.[12]

2.3.5 Model Simulations

In this study we first sought to quantify (1) the contribution of SGLT2 to PT sodium reabsorption under normal conditions, (2) the degree to which PT sodium reabsorption through SGLT2 is increased in diabetes, and (3) the reduction in PT sodium reabsorption due to SGLT2 inhibition. Glucose and sodium filtration, reabsorption, and excretion over the course of a day were simulated in a healthy, controlled T2DM (cT2DM), and uncontrolled T2DM (uT2DM) virtual patient given 3 doses of 100 g glucose throughout the day, representing a standard meal. Parameters for the cT2DM virtual patient were determined from the model fitting described above. To simulate uT2DM, the cT2DM virtual patient was then modified by increasing baseline plasma glucose to 280 mg/dL. Filtered glucose load, glucose reabsorption, and glucose excretion were simulated for each case. Total sodium reabsorption through SGLT2, as well as the fraction of filtered sodium reabsorbed through SGLT, was determined according to equations 2.9 and 2.7, respectively.

To evaluate the effect of SGLT2 inhibition on PT sodium reabsorption, we then repeated these simulations in the cT2DM virtual patient, with and without a dose of canagliflozin 300 mg (as modeled by setting RT_G to the corresponding estimated value for that dose).

2.3.6 Software Implementation

The model was implemented in Berkeley Madonna (version 8.3.18; University of California, Berkeley, California). Model code is provided in the supplement. Data from the studies[11,12] were digitized from the published figures using Matlab (Mathworks, Natick, Massachusetts).

2.4 RESULTS

Estimated model parameter values for cT2DM, fit to the placebo arm of Devineni et al,[12] are given in Table 2.1. All other parameter values were taken from Jauslin et al.[8-10] The estimated values for glucose-dependent insulin clearance, rate of insulin effectiveness, and S_{inc} differed but were of the same order of magnitude as previously estimated values. The baseline glucose levels in Devineni et al were higher than in Jauslin et al, suggesting that patients in the Devineni study were more severely diabetic. The lower estimated values for glucose-dependent insulin clearance and the rate of insulin effectiveness, which together represent sensitivity to insulin, as well as S_{inc}, which represents the incretin response to glucose intake, are consistent with a more severely diabetic population. The estimated values for RT_G at each dose were very similar to those determined by Devineni et al[12] (see Table 2.2).

As shown in Figure 2, the updated model was able to describe the data for both plasma glucose and 24-hour UGE in T2DM patients on placebo and 3 doses of canagliflozin. A single parameter change—lowering RT_G to represent SGLT2 inhibition—was sufficient to describe not only dose-dependent changes in UGE but also the resulting reductions in plasma glucose. The estimated values for RT_G at each dose were similar to those determined by Devineni et al[12] (see Table 2.2).

2.4.1 Contribution of SGLT2 to PT Sodium Reabsorption Under Normal and Diabetic Conditions

Figure 2.3A-C shows the simulated renal filtered glucose load over 24 hours in healthy, cT2DM, and uT2DM virtual patients. As long as the filtered load is below RC, all filtered glucose is reabsorbed. When filtered glucose exceeds RC, the excess glucose is excreted. Thus, the area under both the filtered glucose and RC curves (shaded in blue) is the total amount of glucose reabsorbed in the PT over 24 hours. The area between the filtered glucose and RC curves (shaded in orange) is the total amount of glucose excreted. Figure 3E and F compares the cumulative 24-hour glucose excretion and reabsorption, respectively, for each case. Because SGLT2 reabsorbs glucose and sodium at a 1:1 molar ratio, Figure 2.3F also represents sodium reabsorption through SGLT2. Figure 2.3G shows the percentage of total filtered sodium that is reabsorbed through SGLT2 in each case.

In healthy volunteers, filtered glucose remains well below RC at all times, and thus, no glucose is excreted; all is reabsorbed. In cT2DM, filtered glucose is higher, but RC is also higher, and the capacity is only exceeded for short periods of time following each meal. Thus, nearly all the filtered glucose load is still reabsorbed. In fact, in the cT2DM case, glucose reabsorption, and thus sodium reabsorption through SGLT2, is twice that of the healthy case (1614 vs 804 mmol/24 h). Glucose excretion in this case is nonzero but fairly small — 46 mmol/d, or about 9 g/d.

In uT2DM the filtered glucose load is higher, but because the filtered glucose load exceeds the RC for longer periods of time after each meal, most of the additional filtered glucose is excreted rather than reabsorbed. The 24-hour UGE is increased 4.6-fold compared to the

cT2DM case (219 vs 27 mmol/d, or 42 vs 9 g/d). But the increase in reabsorbed glucose and sodium is only increased by 20%: 1908 vs 1614 mmol/d.

As a fraction of total filtered Na load, in the healthy virtual patient, 5.7% of filtered Na is reabsorbed through SGLT2. In the cT2DM case, this doubled to 11.5%. In uncontrolled diabetes this increased a little further, to 13.7%. Because the PT reabsorbs 60% to 80% of the filtered sodium load, this means that 7.1% to 9.5%, 14.4% to 19.2%, and 17.1% to 22.8% of sodium reabsorption in the PT is due specifically to SGLT2, in the healthy, cT2DM, and uT2DM virtual patient, respectively.

Table 2.1. Estimated Model Parameters for cT2DM and Comparison with Previously Determined Values

Parameter	Description	Value	Previous Value
CL_{GI}, (L/min)/(mIU/L)	Insulin-dependent glucose clearance	0.0024	0.0059
k_{IE}, /min	Rate constant for insulin effect compartment	0.0077	0.0213
S_{inc}, 1/mmol	Slope of effect of glucose absorption on insulin release (incretin effect)	0.076	0.18
RT_G, mmol/L	Renal threshold for glucose excretion	13.5	N/A
G_{SS}, mmol/L[a]	Initial glucose concentration	11.3	8.8
I_{SS}, mIU/L[a]	Initial insulin concentration	13.5	8.6
GFR (mL/min)[a]	Glomerular filtration rate	110	
C_{Na} (mEq/L)[a]	Plasma sodium concentration	140	

Previous data are from Jauslin et al.[8-10] Parameters unchanged from Jauslin et al are not shown.
[a]Parameters taken from Devineni et al,[12] rather than estimated.

Table 2.2. Estimated Values of Renal Threshold for Glucose Excretion and Renal Capacity for Glucose Reabsorption Following Treatment with SGLT2i Canagliflozin Compared with Reported Values

Parameter	Definition	Placebo	Cana 50 mg	Cana 100 mg	Cana 300 mg
RT_G,mg/dL (mmol/L), estimated	Renal threshold for glucose excretion	244 (13.5)	148 (8.2)	106 (5.9)	99 (5.5)
RT_G,mg/dL, reported[12]		235	143	97.5	104
RC (mmol/h), calculated	Renal capacity for glucose reabsorption	89	54	38	36.3

Cana indicates canagliflozin.

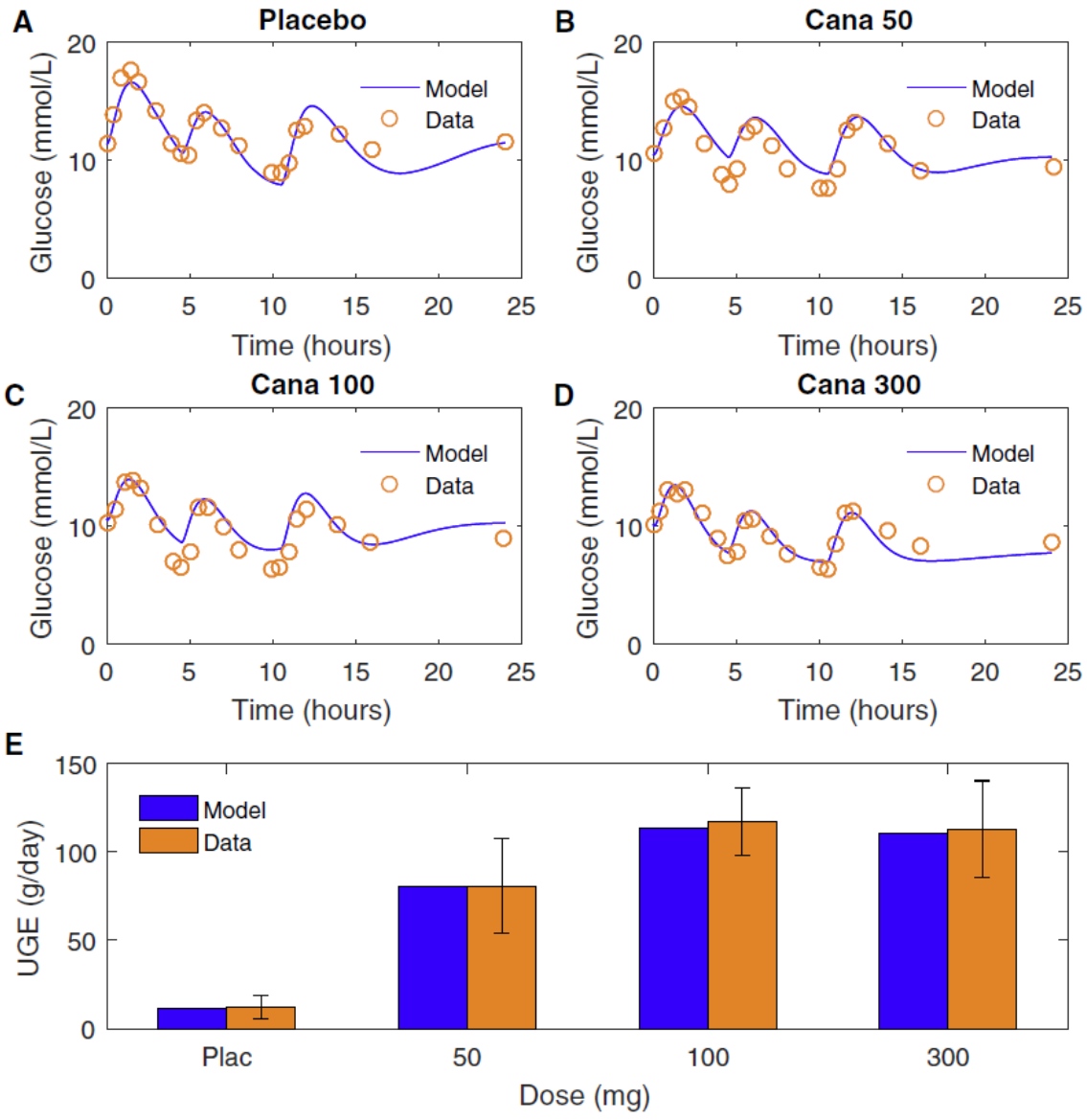

Figure 2.2. The model describes the glucose concentration-time profile (**A-D**) and 24-hour UGE (**E**) in T2DM patients on placebo or 50, 100, or 300 mg canagliflozin.[12] Cana indicates canagliflozin; T2DM, type 2 diabetes mellitus; UGE, urinary glucose excretion.

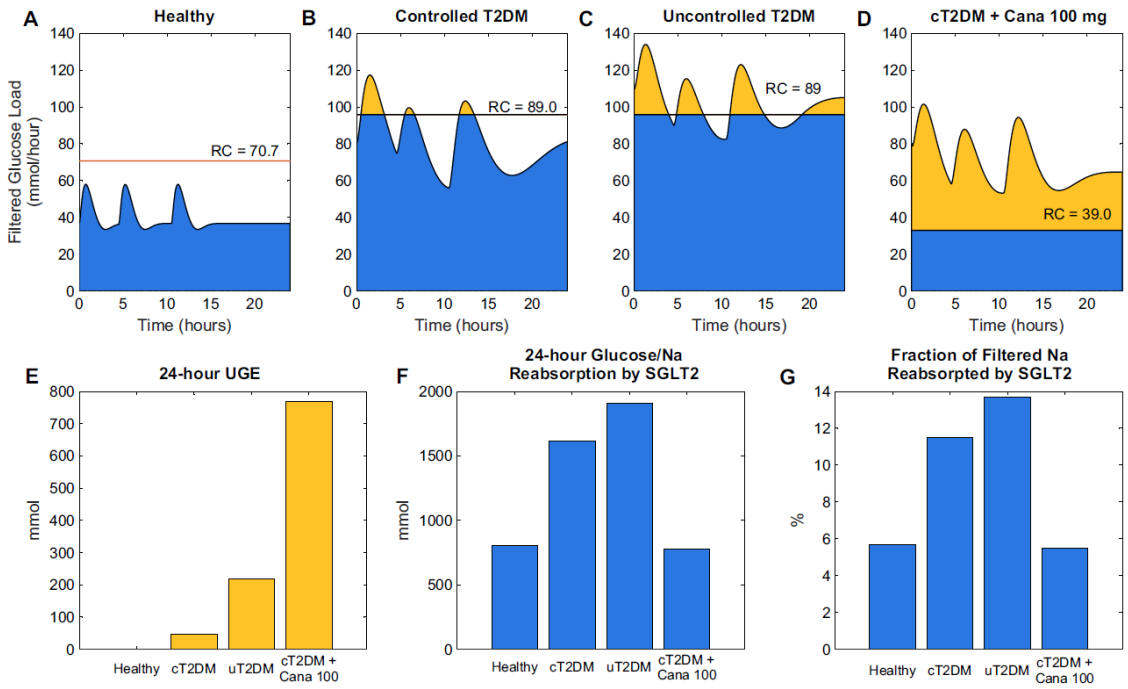

Figure 2.3. A-D, Filtered glucose load in (**A**) healthy, (**B**) controlled T2DM, (**C**) uncontrolled T2DM, and (**D**) controlled T2DM treated with 100 mg canagliflozin. **E**, Twenty-four-hour UGE (equal to orange area in **A-D**). F, Twenty-four-hour cumulative glucose (equal to blue area in **A-D**). Also represents sodium reabsorption through SGLT2 because sodium and glucose are reabsorbed at a 1:1 molar ratio. **G**, Percentage of total filtered Na load that is reabsorbed through SGLT2. Blue shaded area indicates total amount of glucose reabsorbed. Orange shaded area indicates total amount of glucose excreted. Cana indicates canagliflozin; cT2DM, controlled type 2 diabetes mellitus; RC, renal capacity for glucose reabsorption; uT2DM, uncontrolled type 2 diabetes mellitus; UGE, urinary glucose excretion.

2.4.2 Effect of SGLT2 Inhibition on PT Sodium Reabsorption

Figure 3D shows the filtered glucose load in the cT2DM virtual patient when the RC has been lowered by treatment with canagliflozin 100 mg. Treatment with canagliflozin lowers RT_G and RC, resulting in more excretion (orange) and less reabsorption of glucose (blue) compared to the cT2DM case without canagliflozin (Figure 2.3B). Because more glucose is excreted, it also mitigates the postprandial rise in glucose. The 24-hour UGE is increased from 46 mmol/d (9 g/d) to 630 mmol/d (121 g/d) (Figure 2.3E). Importantly, glucose and sodium reabsorption through SGLT2 are restored to normal levels (Figure 2.3F, G).

2.5 DISCUSSION

This study quantified the contribution of SGLT2 to renal sodium reabsorption in health and disease and following treatment with an SGLT2 inhibitor. In the healthy state, SGLT2 accounts for a relatively small fraction of total sodium reabsorption (about 6%), although it represents a slightly larger contribution to PT-specific sodium reabsorption (7% to 9%). In the diabetic state, when blood glucose levels are increased to near RT_G, this contribution is doubled to around 12% of total, or 14% to 19% of PT sodium reabsorption. These values are consistent with previous studies showing that PT sodium reabsorption is increased 5% to 25% in diabetes.[4-6] Treatment with an SGLT2i normalizes the fraction of sodium reabsorption through SGLT2.

Increased PT sodium reabsorption affects GFR and glomerular capillary hydrostatic pressure in several ways. First, increased PT reabsorption reduces sodium flow through the macula densa, stimulating tubuloglomerular feedback that dilates the afferent arteriole and increases glomerular hydrostatic pressure.[2] Second, increased PT sodium reabsorption reduces fluid flow through the PT and thus reduces Bowman's space pressure that opposes filtration.[2,5,13] Third, as we have recently illustrated mathematically,[3] an increase in PT sodium reabsorption causes a sodium imbalance, which must be corrected. Under normal conditions, sodium reabsorption through other transporters along the nephron may be downregulated to compensate and restore sodium balance. However, when this compensatory downregulation is impaired, the only remaining way to restore sodium balance is by increasing filtration. As long as a sodium balance persists, sodium and fluid accumulate, increasing blood pressure, glomerular hydrostatic pressure, and GFR until the point that sodium excretion again matches intake. Our previous simulations suggest that a 7% to 10% increase in PT sodium reabsorption would be sufficient to cause elevation in glomerular hydrostatic pressure, especially if coupled with impairment in

distal regulation of sodium reabsorption—a common feature in diabetes. Coupled with our previous work, the current study confirms that the magnitude of increase in sodium reabsorption due to SGLT2 is likely sufficient to produce pathologic changes in glomerular hemodynamics.

It may seem counterintuitive that sodium retention is increased in diabetes because diabetes is often associated with excess urine production and dehydration. However, these periods of dehydration usually occur when blood glucose levels have become excessively elevated. Our simulations demonstrate that during periods of uncontrolled hyperglycemia, as blood glucose rises above RT_G, the capacity of SGLT2 for glucose (and sodium) reabsorption is exceeded, and most of the excess glucose is excreted in the urine, so that there is only a small additional increase in sodium reabsorption through SGLT2. At the same time, because there is substantial glucosuria in the uncontrolled state, we can speculate that osmotic diuresis and associated solvent drag may actually lead to an overall reduction in sodium reabsorption (and increase in excretion) in this case. In other words, as long as glucose levels in the diabetic patient remain at or below RT_G, there is overall sodium retention due to SGLT2, but as glucose rises above RT_G, SGLT2-related sodium retention may be countered by losses due to osmotic diuresis, leading to polyuria and dehydration.

In these simulations, we assumed that all additional glucose reabsorption in diabetes is through SGLT2. However, although SGLT1 normally reabsorbs only 3% to 10% of filtered glucose, in diabetes, when the glucose reabsorption capacity of SGLT2 is surpassed and the load of glucose reaching the S3 segment increases, there is likely some compensation through increased SGLT1 reabsorption. The increase in renal threshold for glucose excretion from about 150 mg/dL in nondiabetics to about 250 mg/dL in diabetics is likely due to a combination of proximal tubular growth and increased SGLT2 density but also increased SGLT1 activity.

Because the degree of compensation through SGLT1 is difficult to distinguish from these other factors, the current model did not attempt to model SGLT1 compensation. However, we can deduce that because SGLT1 reabsorbs sodium and glucose at a 2:1 molar ratio, compared to the 1:1 molar ratio for SGLT2, any portion of the increase in glucose reabsorption from the normal to diabetic state due to increased reabsorption through SGLT1 rather than SGLT2 would result in an even higher increase in sodium reabsorption. Therefore, the increase of 12% calculated here is a lower bound.

Our results also indicate that treatment with an SGLT2 inhibitor such as canagliflozin normalizes the contribution of SGLT2 to tubular sodium reabsorption. By normalizing PT sodium reabsorption, an SGLT2i may indirectly reduce glomerular capillary hypertension and slow the rate of renal injury. This is consistent with the GFR response observed in the EMPA-REG trial.[7] An acute reduction in GFR (over the first few weeks of the trial) was observed, consistent with a hemodynamic response to the drug (ie, lowering of glomerular pressure), followed by a much slower rate of GFR decline compared to placebo. In addition, SGLT2 inhibitors have been shown to reduce proteinuria,[14] another indication of lowering of glomerular hypertension. In addition to direct effects on PT sodium reabsorption, the glucosuria caused by SGLT2 inhibitors induces an osmotic diuresis effect, which may further contribute to excess sodium and water excretion and subsequently alter systemic and renal hemodynamics. In this study, we could not evaluate the osmotic diuresis contribution of SGLT2i on sodium reabsorption.

Because we did not directly account for possible compensatory reabsorption through SGLT1 in the model, we also must consider whether SGLT1 compensation might impact the true effect of SGLT2 inhibition on decreasing sodium reabsorption. We do not believe this is the case

for the following reason. Even controlled diabetics tend to have levels of glucose excretion that are measurably larger than in nondiabetics, and increases in plasma glucose are associated with increases in glucose excretion. This suggests that even with a compensatory increase in renal threshold for glucose excretion, diabetic patients operate near saturation of both SGLT1 and SGLT2 transporters. Further increases in blood glucose levels result in excess filtered glucose that neither SGLT1 nor SGLT2 transporters are able to reabsorb. Therefore, it follows that when an SGLT2 inhibitor is given, the amount of glucose reaching the SGLT1 in the S3 will increase, but because SGLT1 transporters are already reabsorbing their maximum capacity, their ability to compensate further is likely small. Therefore, we believe that the model-predicted effects of SGLT2 inhibition on sodium and glucose reabsorption are accurate. Still, it should be noted though that although SGLT1 are likely already saturated and do not compensate under SGLT2 inhibition, a therapy that inhibits both SGLT1 and SGLT2 would be expected to further increase glucose excretion. As illustrated in Figure 2.3E, there is still substantial glucose reabsorption during treatment with canagliflozin. This may be due to incomplete SGLT2 suppression, reabsorption by SGLT1, or both. A dual inhibitor would potentially increase glucose excretion further and, because of the 2:1 sodium glucose ratio of SGLT1 inhibitors, would have an even greater impact in reducing sodium reabsorption than a selective inhibitor.

In this study we assumed a normal GFR in all cases. The level of GFR determines the filtered glucose and sodium load and thus will affect total amount of sodium reabsorbed. Early diabetes is frequently characterized by renal hyperfiltration. In hyperfiltering patients, the filtered glucose load, and thus the predicted increases in glucose and sodium reabsorption, could be even higher. In diabetics who develop chronic kidney disease, GFR declines, but single-nephron GFR increases as the remaining uninjured nephrons try to compensate for lost nephrons. This may

also affect the dynamics of glucose and sodium reabsorption. In future work, by coupling the glucose-insulin dynamics model with a model of renal hemodynamics, we plan to evaluate the impact of renal hyperfiltration as well as the consequences of a decline in GFR, as nephrons are lost, on sodium reabsorption through SGLT2.

We focused in this study on quantifying the contribution of SGLT2 on proximal sodium reabsorption in diabetes and the impact of SGLT2i in reducing it because of the increasingly recognized role of increased proximal reabsorption in glomerular hypertension and subsequent renal damage. However, SGLT2 inhibitors may have favorable effects on renal function through other mechanisms as well. By reducing proximal reabsorption, they may favorably alter oxygen consumption along the nephron.[15] They have also been shown to reduce inflammation and tubular fibrosis. This may be an indirect effect of improved renal hemodynamics and reduced proteinuria and oxygen consumption but could also be an independent effect of SGLT2 inhibitors.[16] Further mechanistic studies, as well as long-term outcomes studies investigating renal end points, are needed to more fully understand the renoprotective effects of SGLT2 inhibitors.

In this work we expanded an established model of glucose and insulin dynamics to account for glucose clearance through urinary glucose excretion. We demonstrated that by changing only a single parameter, RT_G, the model was able to reproduce the reduction on blood glucose observed with the SGLT2 inhibitor canagliflozin. To our knowledge, this is the first model to mechanistically incorporate renal clearance of glucose in a model of glucose dynamics. Although under normal conditions, renal clearance of glucose is negligible, this is an important clearance route in uncontrolled diabetes and during treatment with an SGLT2i. Thus, this model

expansion may be useful beyond the current questions, when considering glucose dynamics in diabetics and/or under SGLT2i.

2.6 REFERENCES

1. Bjornstad P, Bjornstad P, Snell-Bergeon JK, et al. Rapid GFR decline is associated with renal hyperfiltration and impaired GFR in adults with Type 1 diabetes. *NEPHROLOGY DIALYSIS TRANSPLANTATION.* 2015;30(10):1706-1711.
2. Vallon V, Thomson SC. Renal Function in Diabetic Disease Models: The Tubular System in the Pathophysiology of the Diabetic Kidney. In. United States: ANNUAL REVIEWS INC; 2012:351.
3. Hallow KM, Gebremichael Y, Helmlinger G, Vallon V. Primary proximal tubule hyperreabsorption and impaired tubular transport counterregulation determine glomerular hyperfiltration in diabetes: a modeling analysis. *American Journal of Physiology (Consolidated).* 2017(5):819.
4. Vallon V, Blantz RC, Thomson S. Homeostatic efficiency of tubuloglomerular feedback is reduced in established diabetes mellitus in rats. In. United States: AMERICAN PHYSIOLOGICAL SOCIETY; 1995:F876.
5. Vallon V, Richter K, Blantz RC, Thomson S, Osswald H. Glomerular Hyperfiltration in Experimental Diabetes Mellitus: Potential Role of Tubular Reabsorption. In. United States: WILLIAMS & WILKINS; 1999:2569.
6. Hannedouche TP, Delgado AG, Gnionsahe DA, Boitard C, Lacour B, Grünfeld JP. Renal hemodynamics and segmental tubular reabsorption in early type 1 diabetes. *Kidney International.* 1990;37(4):1126-1133.
7. Wanner C, Inzucchi SE, Lachin JM, et al. Empagliflozin and Progression of Kidney Disease in Type 2 Diabetes. *New England Journal of Medicine.* 2016;375(4):323-334.
8. Jauslin PM, Silber HE, Frey N, et al. An integrated glucose-insulin model to describe oral glucose tolerance test data in type 2 diabetics. *Journal of Clinical Pharmacology.* 2007(10):1244.
9. Jauslin PM, Frey N, Karlsson MO. Modeling of 24-Hour Glucose and Insulin Profiles of Patients With Type 2 Diabetes. *The Journal of Clinical Pharmacology.* 2011;51(2):153-164.
10. Silber HE, Jauslin PM, Frey N, Gieschke R, Simonsson USH, Karlsson MO. An Integrated Model for Glucose and Insulin Regulation in Healthy Volunteers and Type 2 Diabetic Patients Following Intravenous Glucose Provocations. *The Journal of Clinical Pharmacology.* 2007;47(9):1159-1171.
11. Sha S, Devineni D, Ghosh A, et al. Canagliflozin, a novel inhibitor of sodium glucose co-transporter 2, dose dependently reduces calculated renal threshold for glucose excretion and increases urinary glucose excretion in healthy subjects. *DIABETES OBESITY & METABOLISM.* 2011;13(7):669-672.
12. Devineni D, Curtin CR, Murphy J, et al. Pharmacokinetics and Pharmacodynamics of Canagliflozin, a Sodium Glucose Co-Transporter 2 Inhibitor, in Subjects With Type 2 Diabetes Mellitus. *JOURNAL OF CLINICAL PHARMACOLOGY.* 2013;53(6):601-610.
13. Vallon V, Blantz RC, Thomson S. Glomerular hyperfiltration and the salt paradox in early [corrected] type 1 diabetes mellitus: a tubulo-centric view. *Journal Of The American Society Of Nephrology: JASN.* 2003;14(2):530-537.
14. Petrykiv SI, Laverman GD, Zeeuw Dd, Heerspink HJL. The albuminuria lowering response to dapagliflozin is variable and reproducible between individual patients. *Diabetes, Obesity & Metabolism.* 2017.

15. Layton AT, Vallon V, Edwards A. Predicted consequences of diabetes and SGLT inhibition on transport and oxygen consumption along a rat nephron. *AMERICAN JOURNAL OF PHYSIOLOGY-RENAL PHYSIOLOGY*. 2016;310(11):F1269-F1283.
16. Fioretto P, Zambon A, Rossato M, Busetto L, Vettor R. SGLT2 Inhibitors and the Diabetic Kidney. *Diabetes Care.* 2016;39(Supplement 2):S165.

CHAPTER 3

DETECTION OF PHYSIOLOGICAL PERTURBATIONS VIA HIGH FREQUENCY TELEMETRY DATA. A CASE STUDY OF MALARIA[1].

---

[1]Jessica A. Brady, Zerotti L. Woods, Saeid Safaei, Jeremy D. DeBarry, Mustafa V. Nural, Jay C. Humphrey, Alberto Moreno, Monica Cabrera-Mora, Elizabeth D. Trippe, Diego Moncada, Regina J. Cordy, Ebru Karpuzoglu, Jianlin Jiang, Jennifer S. Wood, Jessica C. Kissinger, The MaHPIC/HAMMER Consortia, Rabindra Tirouvanziam, Mary R. Galinski, and Juan B. Gutierrez. To be submitted to *Nature Methods*.

3.1 ABSTRACT

Early detection of physiological changes due to infectious diseases could guide treatment prior to the onset of symptoms and pathogenic consequences. Here we developed telemetry methods to detect and monitor physiological changes in nonhuman primates prior to and in the course of infectious disease progression, specifically malaria. Current malaria diagnostic tests, generally used once a patient has symptoms, confirm the presence of infections caused by malaria parasites in the blood. We analyzed high-frequency physiological data captured from telemetry devices implanted in *Macaca mulatta* and *M. fascicularis* prior to and after infection with *P. knowlesi* sporozoites. Our results show for the first time that host physiological perturbations can be detected while malaria parasites are multiplying in the liver, a step that precedes blood-stage infections and symptomology. These data provide an impetus for the development of novel preemptive telemetry systems for the diagnosis of malaria and possibly other infectious diseases.

3.2 INTRODUCTION

Early and accurate detection of the physiological changes due to pathogenesis of infectious disease can help ensure rapid treatment prior to, or during, the onset of symptoms. Early treatment may reduce the prospects for complications[1,2,3], and can lead to a decrease in transmission of the infectious disease, thus protecting others in the community. Inflammatory processes due to infection can be detrimental or beneficial to the host depending upon their intensity and duration[4]. Timely detection of infection may allow for the development of strategies to control the imbalance of inflammatory processes thus decreasing risk for further complications.

Current methods for early diagnosis vary and have known limitations. Imaging[5], polymerase chain reaction (PCR)-based diagnostics[6], rapid molecular detection[7], and immunologic tests[8] are among some of the tools used to detect infectious diseases. Imaging has been used in conditions that cause damage greater than the spatial resolution of the technology of choice, e.g. > 1mm using T4 MRI[9]. PCR-based diagnostics are effective for a variety of infectious diseases but require that pathogens be present in the tissue type or sample studied, e.g. mouth swab, blood[1], etc. Rapid molecular detection assays rely on non-invasive collection of samples, e.g. nose swab[10], sputum[7], etc., but not all pathogens are present in those easily accessible samples. Immunologic assays have been useful for diagnosis, and require an understanding of the immunologic responses expected and the antigen or antibody specific to a disease; however, antigen recognition is, in some cases, broad and highly variable from individual to individual[8]. Overall, current methods for diagnosis of infectious diseases are limited by the amount of time required to process results, further tests required to confirm diagnosis to administer the correct treatment[1], and test sensitivity.

In this study, we overcome limitations of current diagnostic methods using telemetry devices. They provide a unique perspective on physiological signals through high frequency sampling rates and continuous measurements. Telemetry systems capture data produced by sensors via electrical signals which are converted and recorded as digital data[11]. Possible measures can include temperature[12], activity[13], electrocardiogram (ECG)[14], electroencephalogram (EEG)[15], oxygen concentration[16], and others. These signals can be captured through an extrinsic system, or via surgically implanted intrinsic devices. Captured data can be used to characterize the health status of a subject. Implantable telemetry devices have been employed to investigate physiological status in clinical settings, disease progression[17], and vaccine reactogenicity[18]. For example, telemetry implants in cynomolgus monkeys allowed researchers to obtain continuous hemodynamic parameters in a dose toxicity study that would have been otherwise impossible to obtain from a freely-moving nonhuman primate[19]. Absence of data related to rapid physiological changes can lead to an incomplete or inaccurate understanding of an individual's health or disease state; these data can only be obtained and quantified with continuous data capturing systems[20].

The high frequency sampling of these physiological signals enables detection of disease signs that may have been missed otherwise. Telemetry devices have been used to characterize infectious disease signs and detect early infection (REF?). Temperature captured via telemetry in nonhuman primates has been explored to identify aerosol-exposure to brucellosis and Venezuelan equine encephalitis virus [21,22]. In murine models, body temperature has been identified as an early indicator of mortality for staphylococcal enterotoxic shock[23]. Telemetric recordings in marmosets after inoculation of dengue virus showed an induced fever and decrease in activity[24]. Temperature changes in nonhuman primates have been explored as an early

identifier for Ebola Virus Infection[25]. Temperature and activity data obtained through biosensors has been used for early detection of infection in pigs[26].

The study of telemetry signals is the study of time series. Frequency analysis of time-dependent signals can characterize biological rhythms and detect when perturbations, also called chronodisruptions[27,28], occur, indicating disease or disease risk for an individual[29-31]. The maintenance of these biological rhythms, especially sleep structure, is important for immune function[32]. When rhythm parameters differ from baseline for an individual, this may indicate disease risk[29].

3.2.1 Case Study: Early detection of infection in malaria

Malaria was responsible for approximately 219 million (95% CI: 203-262 million) cases in 2017, with 92% occurring in the African region alone[33]. Immediately after entering a host via mosquito inoculation, *Plasmodium* parasites travel to the liver where they infect hepatocytes and multiply significantly. During the liver stage, the host does not experience symptoms, thus parasite presence often goes undetected. After multiplying in the liver for a number of days (based on the parasite species[34]), parasites enter the bloodstream where they begin an exoerythrocytic cycle of red blood cell infection, multiplication, and rupture. As parasites multiply in the blood, symptoms may occur and malaria diagnosis can be made[35]. Symptoms of *Plasmodium* infection include fever, chills, muscle aches, headache, nausea, and vomiting among others[36], which can be misdiagnosed in the absence of a formal malaria diagnostic test, potentially leading to inappropriate and ineffective treatment for this disease.

Current commercial diagnostic technologies are limited to the blood stage of an infection and are generally used once a person has symptoms typical of malaria. Such diagnostic methods

include the current gold standard of laboratory diagnosis by detecting infected red blood cells by microscopy, rapid diagnostic tests that detect parasite proteins or byproducts in blood samples[37,38], and PCR tests that confirm the parasite's presence in the blood[6,39]. Newer methods include imaging flow cytometry to detect the erythrocytic stage[40] and breathalyzers, which can detect malaria-associated biomarkers and mosquito attractants; these have not been made commercially available yet[41]. However, there is still a critical delay of many days from the time of sporozoite inoculation and liver infection until these blood-based detection methods can be effective.

In this study, we captured high frequency physiological data from implanted telemetry devices in two species of macaques (*Macaca mulatta* and *M. fascicularis*) infected with *Plasmodium knowlesi*. We detected biological rhythm disruptions that differentiate pre-infection periods from the liver stage. The telemetry devices were turned on for a baseline pre-infection period, and through the course of longitudinal infections. Our methods and results showcase this emerging technology and highlight its potential application for disease diagnostics and use in public health management.

3.3 METHODS/RESULTS

3.3.1 Custom automated telemetry system, high-volume continuous data transfer, and analysis overview

We designed and implemented an automated system to collect, store, and analyze telemetry data, approximately 2.5 terabytes (Fig. 3.1). Temperature, activity, blood pressure, and electrocardiogram (ECG) measures were obtained from a cohort of six *M. mulatta* and seven *M. fascicularis* through implantable telemetry devices to capture nearly uninterrupted data (1 -1000

Hz, see Table 3.1) during the pre-infection baseline period (days -10 – 0) and the longitudinal infection period (days 1 – 10), which was initiated by the inoculation of *P. knowlesi* sporozoites. Additional information related to the surgical procedure can be found in the Online Methods.

An L11 Physiotel Digital implant device[42] that captures ECG, temperature, blood pressure, and activity was surgically inserted into the abdomen of the nonhuman primates (NHPs) (see surgery information in Online Methods). The device contained sensors for temperature, three orthogonal accelerators, a catheter that allowed for blood pressure readings, and biopotential leads enabling ECG capture. All variables were sampled according to the frequencies found in Table 3.1.

Table 3.1: Experimental Details and Sampling Frequencies per Physiological Variable.

			Sampling Frequencies			
Experiment ID	**Host Species**	**Number of Subjects**	**Temperature**	**ECG**	**Accelerometer (X,Y,Z)**	**Blood Pressure**
E30	*M. mulatta*	2	1 Hz	1000 Hz	10 Hz	1000 Hz
E07B	*M. fascicularis*	7	1 Hz	1000 Hz	10 Hz	500 Hz
E06	*M. mulatta*	4	1 Hz	1000 Hz	10 Hz	500 Hz

A

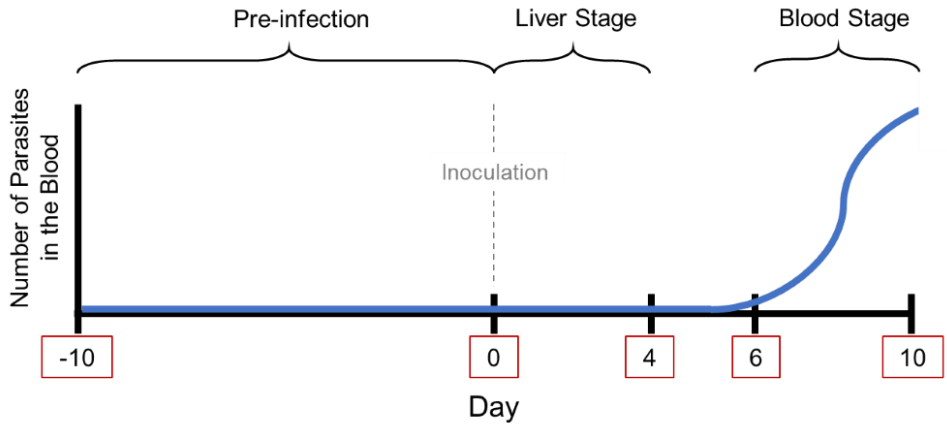

B

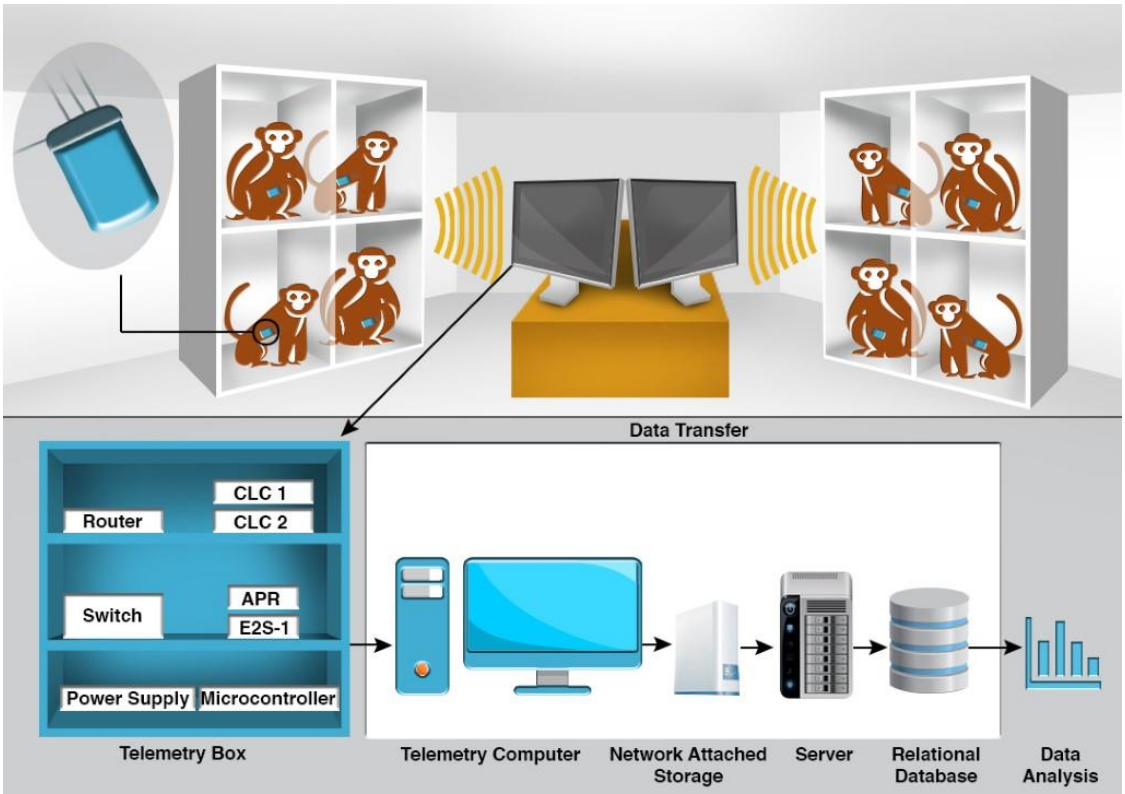

Figure 3.1: Experimental design and data transfer process. (**A**) Idealized experimental timeline with infection stage indications. The liver stage determination day range is described in the Online Methods. (**B**) Overview of data acquisition, transfer, and storage processes, starting from the telemetry device ending in data analysis. See Online Methods for more details.

3.3.2 Hardware

The signal from the telemetry implants was transmitted through radiofrequency and detected by receivers, connected to corresponding components from a vendor[42], that transferred the data to the ‘telemetry computer’ dedicated for collection of these data (Fig. 3.1B). A barometric pressure sensor was in the same facility where the nonhuman primates were located, capturing data at 1 Hz.

3.3.3 Data Transfer

It was necessary to architect and implement a custom software solution to parse the data because, at the time of this study, no vendor's software could export it at full sampling frequency in real-time (see Online Methods for details). Furthermore, our solution efficiently merged the operations of parsing raw data files and loading a relational database. Raw files were retained in an iRODS-managed file repository (https://irods.org/).

To protect against data loss, all files were retained on the telemetry computer until the conclusion of each experiment (Table 3.1) and confirmation that all files were transferred to the centralized server. As a second safeguard to protect against data loss due to possible damage of the telemetry computer, all files were also archived on a network-attached storage until the end of each experiment and the same confirmation of transfer. After each experiment, checksums for all files on the telemetry computer were generated and compared to checksums of transferred files at the centralized server.

3.3.4 Data Preprocessing

Data preprocessing refers to the activities involved in filtering outliers, filling in or ignoring systematically missing data, and down-sampling. The data created by the vendor's software reported missing data with a different set number per channel, which allowed us to identify readings that in reality corresponded to missing data.

Averages per minute for each variable type were obtained using the first fifteen seconds of each minute if there was adequate data in that minute interval. The following minute-average features were computed per data type: blood pressure, acceleration, temperature, and ECG R peak. Blood pressure sensors are affected by barometric pressure; to analyze the blood pressure readings, the atmospheric pressure average per experiment was subtracted from the raw blood pressure data. The mean arterial pressure was computed by identifying the average systolic and diastolic pressure and the sum of one-third of the average systolic pressure and two-thirds of the diastolic pressure. The Euclidean norm was computed for accelerometer data in three orthogonal directions to characterize overall changes in activity and the average of the standard deviation of the Euclidean norm was used as a feature for activity.

3.3.5 Multiple-Component Cosinor Model and Statistical Analysis

After each physiological signal was processed and downsampled to obtain minute averages of temperature, R peak height from ECG, mean arterial pressure and standard deviation of activity, these measures were divided into 24-hr intervals. For each individual, daily biological rhythm parameters were estimated using a multiple-component cosinor model and least squares estimation for each data type.

An implementation of the model[43,44] was used with a fundamental circadian period (24-hr) and corresponding harmonics, as illustrated in equation (3.1):

$$y = M + \sum_{k=1}^{3} a_k cos\left(\frac{2\pi kt}{T} + \Phi_k\right), \quad \text{(Eq. 3.1)}$$

where M is the Midline Estimating Statistic of Rhythm (MESOR), the weights a_k are related to the amplitude of the rhythms for different periods, T. The fundamental period of T when $k = 1$ is 24 hours and the ultradian period harmonics are 12 and 8 hours. The phase shifts, Φ_k, are the translations for the cosine waveforms where the reference time is midnight local time. An example of model fit is illustrated in Fig. 3.2.

The daily estimated parameters for an individual per data type were then grouped into pre-infection, liver stage, and blood stage for statistical comparison. Pre-infection was compared to liver stage using the Kruskal-Wallis nonparametric test for the distribution of each parameter, per variable type, per individual. This comparison identified the parameters for which the p-value was less than 0.05 indicating a significant change from baseline. This comparison was also made between pre-infection and blood stage. The statistically significant parameter changes that occurred in different parameters for the two host species are summarized in Table 3.2. These results were validated via statistical comparison between two intervals of pre-infection per individual.

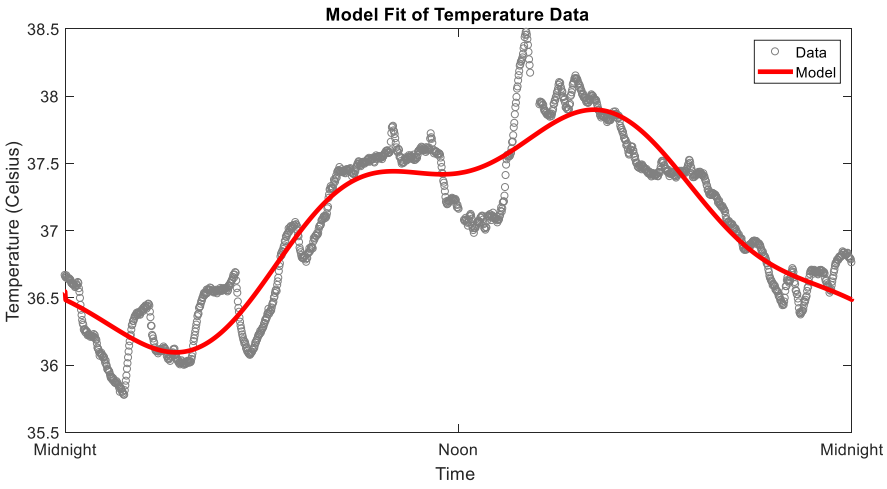

Figure 3.2: Example Model Fit of Temperature Data. Example of temperature data collected for an individual during a day of pre-infection (gray circles) and corresponding multiple-component cosinor model fit (red line).

Table 3.2: **Parameter Comparisons between Pre-infection and Infection Stages using Kruskal-Wallis Test.** Comparisons were made with the pre-infection period data (Pre-) and both liver stage data captured during days 1 – 4 and blood stage data captured during days 6 – 9. A description of the determination of these tissue-specific days of the infections can be found in the Online Methods section. ECG = Electrocardiogram. MESOR = Midline Estimating Statistic of Rhythm. Amp = Amplitude.

	Temperature		ECG – R Peak Height		Mean Arterial Pressure		Activity	
	Pre - Liver	Pre - Blood	Pre - Liver	Pre - Blood	Pre - Liver	Pre - Blood	Pre - Liver	Pre - Blood
***M. mulatta* (n = 6)**	MESOR (3)	MESOR (6)		8hr Amp (4)	8hr Amp (2)	8hr Amp (4) 12hr Amp (4)		MESOR (4) 24hr Amp (5)
***M. fascicularis* (n = 7)**	MESOR (3)	MESOR (6)	MESOR (3)	MESOR (6)	MESOR (7)			

( ) - # of individuals with p-value < 0.05

3.3.6 Classification Analysis Between Pre-Infection and Liver Stage

The feature matrix was obtained from the daily level parameters estimated per data type by the multiple-component cosinor model for all individuals for pre-infection and liver stage. Two machine learning algorithms were implemented for classification between pre-infection baseline and post-infection liver stage with this feature matrix as the input. An overview of the analysis

pipeline can be seen in Fig. 3.3. Online Methods have additional details about the machine learning algorithms used.

The random forest with boosting algorithm aims to create a strong classifier from several weak iterative classifiers. We computed a sequence of simple trees (weak classifiers) where each tree learns from the mistakes of the previous tree, which in turn created a stronger classifier. First, we built a tree model for training data, then created a second tree model which allowed us to correct the errors from the first tree model. We added more decision trees until the boosting decision tree model could predict the training set perfectly, meaning the classification between pre-infection and liver stage on the training data was 100% correct. Using this model, we were able to accurately classify between pre-infection and liver stage days with an average accuracy of 82% on the test data using 10-fold cross-validation.

We implemented a feedforward fully-connected neural network for comparison. The goal of most feedforward networks is to minimize a loss function that is constructed using the comparison of desired outputs of the training set and the actual model output. We used the binary cross entropy function as the loss function. The architecture of the model was 10 layers with the feature matrix as the input. Using 10-fold cross-validation for this model, we obtained an average accuracy of 80% classification between pre-infection and liver-stage days after 200 epochs over the test data.

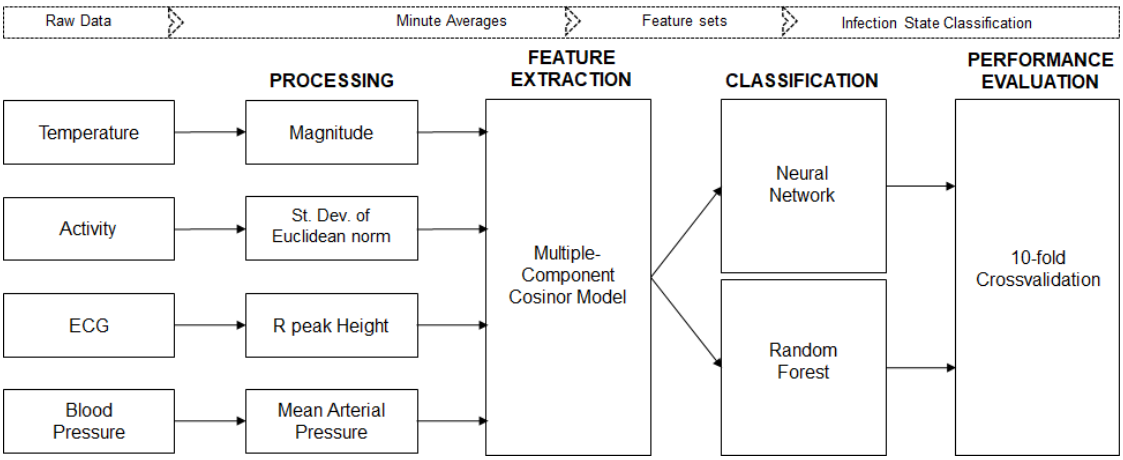

Figure 3.3: Analysis Pipeline Overview. Overview of analysis process from raw data to infection stage classification.

3.4 DISCUSSION

In this study, we implemented a telemetry system, data infrastructure, and analysis pipeline for early detection of physiological changes due to pathogenesis, using malaria as a model. The effectiveness of this system was demonstrated with *P. knowlesi* infection in two species of nonhuman primates, *M. mulatta* and *M. fascicularis*. Physiological signals (temperature, blood pressure, activity, and ECG) were continuously captured and used to characterize baseline biological rhythms and perturbations during infection with *P. knowlesi*.

Our results show that physiological perturbations that were previously uncharacterized are occurring in the host during the liver stage. Using estimated biological rhythm parameters and machine learning algorithms, consensus classification between pre-infection and liver stage was obtained with over 80% accuracy. However, the mechanism of biological rhythm perturbation during the liver stage is unknown; it could be a disruption to the genetic circuits that regulate circadian rhythms or something else entirely [45,46].

We used two different machine learning techniques on this data set to build consensus: artificial neural networks, and random forests. Due to the size of the data set, the neural network

was not consistent over the different validation sets. On some sets in the 10-fold cross-validation we received higher results than others. This could be caused by the neural network not having enough data to fully learn the patterns. However, the random forest method was more consistent over this data set and demonstrated a higher average classification rate. Since both approaches achieved at least 80% accuracy it is likely that with more data, the classification accuracy would be similar if not higher.

We recommend further studies be conducted to investigate what specific interaction causes this chronodisruption, as it may lead to treatment strategy improvements. Since the synchronization of host and parasite rhythms has been identified as an important part of host-parasite interactions[47,48], frequent sampling of telemetry data could provide novel insights into why we were able to use rhythm parameters to distinguish between pre-infection and liver stage[49,50].

Given the relatively low cost of wearable telemetry devices, it is feasible to design a device for mass distribution in malaria endemic regions, to detect infection early and decrease the time to treatment. This intervention could have a profound impact in the control of malaria, and the morbidity and mortality attributed to it, by reducing illness and complications due to the disease, as well as transmission. It has also been suggested that chronotherapy[51] of malaria would inform drug administration to coincide with the time of increased vulnerability of the parasite[52] in the erythrocytic stage.

It is possible that there could exist chronodisruption signatures for other diseases, allowing for earlier and more accurate detection of them as well. Physiological changes due to pathogenesis include conditions that constrain movement, alter temperature, and disrupt sleep patterns, and other changes that can be detected globally with telemetry technology that is

readily available. As the field of precision medicine progresses, our proposed analysis and classification could be used in coordination with pre-existing health monitoring systems if additional clinical studies for validation occurred in the future. More research is needed.

3.5 ONLINE METHODS

3.5.1 Animals

All animal procedures were performed at the Yerkes National Primate Research Center (YNPRC) of Emory University, approved by the Emory University Institutional Animal Care and Use Committee (IACUC), and carried out in accordance with the Animal Welfare Act and Regulations and Public Health Service Policy on the Humane Care and Use of Laboratory Animals.

Yerkes National Primate Research Center is an Association for Assessment and Accreditation of Laboratory Animal Care International (AAALAC)-accredited institution, and all macaques in this study were housed in accordance with standards set forth by the Guide for the Care and Use of Laboratory Animals. Animals were housed indoors in quad-unit stainless steel caging. The animal housing rooms had 12:12h light-dark cycles, with temperature maintained between 65-75 degrees Fahrenheit and humidity kept between 30-70 percent. Animals were fed a commercial monkey chow (LabDiet 5037, LabDiet, St. Louis, MO) supplemented daily with fresh produce, and they had access to water ad libitum.

3.5.2 Surgery and Device Implantation

The animals were anesthetized with Telazol (3-5mg/kg IM) or ketamine (10 mg/kg IM) to facilitate surgical preparation and endotracheal intubation. They were maintained at a surgical

plane of anesthesia with isoflurane inhalant anesthetic mixed with oxygen and received an intravenous infusion of isotonic fluids at 5-10 mL/kg per hour. The PhysioTelTM L11 telemetry implant device[42] was secured between the external and internal abdominal oblique muscles, with the arterial blood pressure catheter inserted into the femoral artery and advanced into the abdominal aorta, and the ECG leads placed in a lead II configuration in subcutaneous pockets on the thorax. Appropriate perioperative medications were given to maintain patient safety and facilitate telemetry device placement. Post-operative medications included flunixin meglumine (1 mg/kg SQ q6h) and buprenorphine (0.01-0.02 mg/kg SQ q6h) for pain management and ceftriaxone (25 mg/kg SQ q24h) to prevent infection. Each animal was allowed at least a two-week recovery period before starting project work.

3.5.3 Study design and experimental infections

The procedures regarding experimental infection of non-human primates with simian malaria parasites have been described in detail elsewhere[53-55]. In this report, we used two species of macaques *M. mulatta* and *M. fascicularis* to assess differences in physiological parameters after experimental infection with *P. knowlesi*. These species of macaques have distinct clinical outcomes when infected with *P. knowlesi*. Infection of the experimental host *M. mulatta* is characterized by the development of high parasitemias that resulted in high mortality. This clinical phenotype of high susceptibility is in contrast with the outcome of the experimental infection of the natural host *M. fascicularis* characterized by the development of self-controlled parasitemias and chronic infections[53-55]. Clinical procedures were approved by the two Institutional Animal Care and Use Committees involved (EMORY IACUC and the Animal Care

and Use Review Office, ACURO, USAMRMC Office of Research Protections), and all the interventions complied with Animal Welfare Act regulations.

Three groups of animals were used for the experiments described here. Six male rhesus macaques (*M. mulatta*) born and raised at the Yerkes National Primate Research Center (YNPRC) were randomized into two groups. 1) Two animals (RKy15 and REd16) were included in the group with the internal code E30, designed to test the effect of subcurative anti-malaria treatment in the susceptible host. 2) Four animals (RCl15, RIh16, RTe16, and RUf16) were included in the group with the internal code E06, designed to study acute infections. The third group comprised seven male long-tailed macaques (*M. fascicularis*) commercially acquired from the Mannheimer Foundation, Inc completed a quarantine period at the YNPRC. These animals were included in the group with the internal code E07b to study chronic infections (H12C8, 11C131, 12C136, H12C59, 12C53, 11C166 and12C44).

Thirty-five to one hundred ten days before experimental infection an L11 telemetry device[42] was surgically implanted between the external and internal oblique muscles. In each animal, the pressure sensor catheter was inserted into the right femoral artery, the ECG negative lead within the right pectoral region and the ECG positive lead at the level of the xiphoid process. Telemetry devices were activated ten to fifteen days before the experimental infection for the collection of physiological data. The *P. knowlesi* PKA+ isolate was used for experimental infections using a single batch of cryopreserved stocks of sporozoites isolated from Anopheles dirus, An. Gambiae, and An. stephensi mosquitoes as described.[53-55] The infectivity of the batch used for the three groups of macaques described here was validated in malaria-naive rhesus macaques. For the experimental challenge and based on results obtained with the dry run infectivity experiments, an estimated number of ~2,500 viable cryopreserved sporozoites were

used for *M. mulatta*, and ~5,000 viable cryopreserved sporozoites were used for *M. fascicularis*, and the parasites inoculated intravenously. Capillary blood samples were obtained every day by standardized ear prick procedures and collected into EDTA-coated capillary tubes starting ten to fifteen days before experimental infection and during the clinical follow-up period after sporozoite inoculation. These samples were used for CBC analyses, parasite counts using Giemsa-stained thin and thick smears, quantification of reticulocytes by manual counting of new methylene blue stained blood smears, and for plasma collection for cryopreservation. Whole blood samples collected from the femoral vein and bone marrow aspirates derived from iliac crest puncture were collected into EDTA-coated Vacutainer tubes at several time points in the course of the experiments. These samples were used for multi-omic analyses including transcriptomics, metabolomics, and immune profiling.

To avoid clinical complications due to the reported virulence of *P. knowlesi* in *M. mulatta* a subcurative treatment with artemether, a fast-acting antimalarial drug, was administered at 2 mg/kg to REd16 eleven days after the experimental infection. None of the other animals received subcurative treatment in the course of the experimental infections. After completion of the clinical follow-up period, the macaques were euthanized and complete necropsy and histopathology analyses performed.

3.5.4 Liver Stage Determination

The liver stage of infection was defined as the period of time between the date of inoculation and two days before the first positive detection of DNA from the parasite in the whole blood. The duration of the liver stage after infection with *P. knowlesi* sporozoites was determined by PCR using the *Plasmodium knowlesi* S1 gene (PKH_080740). A *Plasmodium knowlesi* S1 gene

specific primer set (Forward primer: 5’ TGCGTCAAAGCAAAACGTGG 3’ and Reverse primer: 5’ TGTCAAGACCATTCCCCCTG 3’) was developed. These primers were demonstrated to amplify *P. knowlesi* genes but not host genes using positive and negative blood samples collected from either *M. mulatta* or *M. fascicularis*. To extract DNA from BD microtainer serum separator tubes (SST), a modified Qiagen DNeasy Tissue protocol was used. A pipette tip was used to create an opening in the serum separation gel to enable gDNA extraction. ATL buffer and proteinase k were then added to the tube and allowed to incubate with the blood pellet followed by quick vortexing. The manufacturer’s suggested protocol was then followed for gDNA extraction. After extraction, samples were eluted in 200 µl of buffer, and the AppliedBiosystems’ PowerUp SYBR Green Master Mix was used in the PCR reactions. A fast cycling protocol using the following protocol 1x 50°C 2min, 1x 95°C 2min, 40x 95°C 5sec, 60°C 45sec was used for amplification. Samples that had a detectable Ct were considered positive, and then, validated by performing DNA gel electrophoresis. A water negative control, a parasite negative monkey sample control and a parasite positive monkey sample control were included in each PCR run to serve as positive and negative controls. All reactions were repeated twice.

3.5.5 Custom Software Solution

The commercially available solution did not allow real-time access to high-frequency data. Data were continuously collected from telemetry implant devices via radio transfer to the telemetry computer physically located in the Yerkes National Primate Research Center (YNPRC) at Emory University. Vendor software[42] stored the telemetry data in digital files, one file per subject per hour. An automated Windows Task Scheduler script was executed hourly on the telemetry

computer to transfer all files less than 180 minutes old to the local network attached storage (NAS) at Emory. This ensured files were collected on the NAS roughly as they were generated. Depending on the specific file type, files were generated either once per NHP per experiment or once per NHP per hour (roughly). Files were named for the experiment number, animal code, and (for hourly files) the date and time stamp of the last file modification. Next, an hourly cron job was executed on the NAS that transferred files from the computer receiving locally the signals to a centralized server for analysis via rsync. Checksums were used to ensure file integrity after transfer. An hourly automated email alert was used to track transfers and monitor available disk space. As hourly transfers from the YNPRC were confirmed, custom software automatically extracted each sensor's data stored in the file (ECG, temperature, etc.) as a series of "raw" timestamp-value tuples, e.g. [date+time] [value]" where the actual sampling time and value were derived from the raw values according to the vendor's documentation and loaded into a relational database.

3.5.6 Analysis

All analyses were performed in MATLAB 2018a and Python 3.7.3.

3.5.7 Machine Learning Algorithms

Random forest with boosting as well as a feed forward fully connected neural network were implemented for classification between pre-infection and liver stage. The random forest algorithm using the “Extreme Gradient Boosting” method in Scikit-learn with 10 k-fold cross-validation[56] was implemented. There were several configurations of the number of trees used and maximum depth that demonstrated the highest classification rates. The summary of

configurations and additional details can be found through the link in the Code Availability section.

For the feedforward fully connected neural network, the architecture of the model includes 10 layers with the input layer having 28 neurons. The subsequent layer uses a Rectified Linear (ReLU) activation with 100 neurons, followed by ReLU activation with 50 neurons, hyperbolic tangent (tanh) activation with 30 neuron, ReLU activation with 15 neurons, tanh activation with 25 neurons, ReLU activation with 20 neurons, ReLU activation with 40 neurons, ReLU activation with 25 neurons, a dropout layer with $p = 0.4$, ReLU activation with 30 neurons, a dropout layer with $p = 0.4$, and a sigmoid activation with 1 neuron. We used the binary cross entropy function as the loss function with the adam optimizer with a batch size of 10. Using 10-fold cross-validation and 200 epochs over the data we computed the average accuracy of classification for this method.

3.6 REFERENCES

1. Yang S, Rothman RE. PCR-based diagnostics for infectious diseases: uses, limitations, and future applications in acute-care settings. *The Lancet Infectious Diseases.* 2004;4(6):337-348.
2. Veldhuijzen IK, Toy M, Hahné SJM, et al. Screening and Early Treatment of Migrants for Chronic Hepatitis B Virus Infection Is Cost-Effective. *Gastroenterology.* 2010;138(2):522-530.
3. Gao L, Liu X, Zhang D, et al. Early diagnosis of bacterial infection in patients with septicopyemia by laboratory analysis of PCT, CRP and IL-6. *Experimental and therapeutic medicine.* 2017;13(6):3479-3483.
4. Soares MP, Teixeira L, Moita LF. Disease tolerance and immunity in host protection against infection. *Nature Reviews Immunology.* 2017;17:83.
5. Maschke M, Kastrup O Fau - Forsting M, Forsting M Fau - Diener H-C, Diener HC. Update on neuroimaging in infectious central nervous system disease. (1350-7540 (Print)).
6. Komaki-Yasuda K, Vincent JP, Nakatsu M, Kato Y, Ohmagari N, Kano S. A novel PCR-based system for the detection of four species of human malaria parasites and Plasmodium knowlesi. *PLoS ONE.* 2018;13(1):e0191886.
7. Boehme CC, Nabeta P, Hillemann D, et al. Rapid Molecular Detection of Tuberculosis and Rifampin Resistance. *New England Journal of Medicine.* 2010;363(11):1005-1015.
8. Gennaro ML. Immunologic Diagnosis of Tuberculosis. *Clinical Infectious Diseases.* 2000;30(Supplement_3):S243-S246.
9. Van Riet J, Hill EE, Gheysens O, et al. 18F-FDG PET/CT for early detection of embolism and metastatic infection in patients with infective endocarditis. *European Journal of Nuclear Medicine and Molecular Imaging.* 2010;37(6):1189-1197.
10. Francois P, Pittet D, Bento M, et al. Rapid Detection of Methicillin-Resistant Staphylococcus aureus Directly from Sterile or Nonsterile Clinical Samples by a New Molecular Assay. *Journal of Clinical Microbiology.* 2003;41(1):254.
11. Carden F, Jedlicka RP, Henry R. *Telemetry Systems Engineering.* Boston: Artech House, Inc; 2002.
12. Buchanan H, Phillips JM, Lopez A, Moore WF. Temperature-sensing telemetry system for unrestrained rhesus monkeys (Macaca mulatta). SAM-TR-67-63. *[Technical Report] SAM-TR USAF School Of Aerospace Medicine.* 1967:1-11.
13. Shinkoda H, Matsumoto K, Hamasaki J, Seo YJ. Evaluation of human activities and sleep-wake identification using wrist actigraphy. 1952, 1952.
14. Cohn AE. Newer Aspects and Methods in the Study of the Mechanism of the Heart-Beat. *Proceedings of the American Philosophical Society.* 1914;53(215):287-302.
15. Berger H. Über das Elektrenkephalogramm des Menschen. *Archiv für Psychiatrie und Nervenkrankheiten.* 1929;87(1):527.
16. Matthes K. Untersuchungen über die Sauerstoffsättigung des menschlichen Arterienblutes. *Naunyn-Schmiedebergs Archiv für Experimentelle Pathologie und Pharmakologie.* 1935;179(6):698.

17. Glynn AR, Alves DA, Frick O, et al. Comparison of experimental respiratory tularemia in three nonhuman primate species. *Comparative Immunology, Microbiology and Infectious Diseases.* 2015;39:13-24.
18. Arras M, Glauser DL, Jirkof P, et al. Multiparameter telemetry as a sensitive screening method to detect vaccine reactogenicity in mice. *PLoS ONE.* 2012;7(1):1-9.
19. Niehoff MO, Niggemann B, Sternberg J, Jenkins A, Holbrook M. Measurement of hyper- and hypotension during repeated dose toxicity studies in either freely moving or physically restrained cynomolgus monkeys. *Journal of Pharmacological and Toxicological Methods.* 2014;70:268-275.
20. Downs JC. IOP telemetry in the nonhuman primate. *Experimental Eye Research.* 2015;141:91-98.
21. Yingst SL, Huzella LM, Chuvala L, Wolcott M. A rhesus macaque (Macaca mulatta) model of aerosol-exposure brucellosis (Brucella suis): pathology and diagnostic implications. *Journal of medical microbiology.* 2010;59(Pt 6):724-730.
22. Reed DS, Lind CM, Parker MD, Pratt WD, Sullivan LJ. Aerosol Infection of Cynomolgus Macaques with Enzootic Strains of Venezuelan Equine Encephalitis Viruses. *The Journal of Infectious Diseases.* 2004;189(6):1013-1017.
23. Vlach KD, Boles Jw Fau - Stiles BG, Stiles BG. Telemetric evaluation of body temperature and physical activity as predictors of mortality in a murine model of staphylococcal enterotoxic shock. (1532-0820 (Print)).
24. Omatsu T, Moi ML, Takasaki T, et al. Changes in hematological and serum biochemical parameters in common marmosets (Callithrix jacchus) after inoculation with dengue virus. *Journal of Medical Primatology.* 2012;41(5):289-296.
25. Reisler RB, Yu C, Donofrio MJ, et al. Clinical Laboratory Values as Early Indicators of Ebola Virus Infection in Nonhuman Primates. *Emerging infectious diseases.* 2017;23(8):1316-1324.
26. Martinez-Aviles MA-Ohoo, Fernandez-Carrion E, Lopez Garcia-Baones JM, Sanchez-Vizcaino JM. Early Detection of Infection in Pigs through an Online Monitoring System. (1865-1682 (Electronic)).
27. Erren TC, Reiter RJ. Defining chronodisruption. *Journal Of Pineal Research.* 2009;46(3):245-247.
28. Erren TC, Reiter RJ. Revisiting chronodisruption: when the physiological nexus between internal and external times splits in humans. *Naturwissenschaften.* 2013;100(4):291-298.
29. Halberg F, Cornelissen G, Halberg J, et al. Circadian Hyper-Amplitude-Tension (CHAT): A disease risk syndrome of anti-aging medicine. *Journal of Antiaging Medicine.* 1998(3):239.
30. Halberg F, Cornélissen G, Hillman D, et al. Chronobiologically interpreted ambulatory blood pressure monitoring in health and disease. *Global Advances in Health and Medicine.* 2012;1(2):66-121.
31. Fernandez JR, Hermida RC, Mojon A. Chronobiological analysis techniques. Application to blood pressure. In. Great Britain: Royal Society; 2009:431.
32. Besedovsky L, Lange T, Born J. Sleep and immune function. *Pflugers Archiv.* 2012;463(1):121-137.
33. Organization WH. *World malaria report 2018.* Geneva; 2018.
34. Crutcher JM, Hoffman SL. Malaria. In: S. B, ed. *Medical Microbiology.* 4th ed. Galveston, TX: University of Texas Medical Branch at Galveston; 1996.

35. Graewe S, Stanway RR, Rennenberg A, Heussler VT. Chronicle of a death foretold: Plasmodium liver stage parasites decide on the fate of the host cell. *FEMS Microbiology Reviews.* 2012;36(1):111-130.
36. Phillips MA, Burrows JN, Manyando C, van Huijsduijnen RH, Van Voorhis WC, Wells TNC. Malaria. *Nature Reviews Disease Primers.* 2017;3:17050.
37. Singh B, Daneshvar C. Human infections and detection of Plasmodium knowlesi. *Clinical Microbiology Reviews.* 2013;26(2):165-184.
38. Barber BE, Grigg MJ, Piera KA, et al. Effects of aging on parasite biomass, inflammation, endothelial activation, microvascular dysfunction and disease severity in Plasmodium knowlesi and Plasmodium falciparum malaria. *Journal of Infectious Diseases.* 2017;215(12):1908-1917.
39. Canier L, Khim N, Kim S, et al. Malaria PCR detection in Cambodian low-transmission settings: dried blood spots versus venous blood samples. *The American Journal Of Tropical Medicine And Hygiene.* 2015;92(3):573-577.
40. Dekel E, Rivkin A, Heidenreich M, et al. Identification and classification of the malaria parasite blood developmental stages, using imaging flow cytometry. *Methods.* 2017;112:157-166.
41. Schaber CaK, N. and Bollinger, L. and Trehan, I. and Raman, B. and John, A.O. Breathprinting Reveals Malaria-Associated Biomarkers and Mosquito Attractants. Paper presented at: 66th Annual Meeting of American Society of Tropical Medicine and Hygiene; Nov. 5-9, 2017, 2017; Baltimore, MD.
42. Data Sciences International SP, MN, USA.
43. Bingham C, Arbogast B, Guillaume GC, Lee JK, Halberg F. Inferential statistical methods for estimating and comparing cosinor parameters. *Chronobiologia.* 1982;9(4):397-439.
44. Padhye NS, Hanneman SK. Cosinor analysis for temperature time series data of long duration. *Biological Research For Nursing.* 2007;9(1):30-41.
45. Duguay D, Cermakian N. The crosstalk between physiology and circadian clock proteins. *Chronobiology International.* 2009;26(8):1479-1513.
46. Mayeuf-Louchart A, Zecchin M, Staels B, Duez H. Circadian control of metabolism and pathological consequences of clock perturbations. *Biochimie.* 2017;143:42-50.
47. O'Donnell AJ, Schneider P, McWatters HG, Reece SE. Fitness costs of disrupting circadian rhythms in malaria parasites. *Proceedings of the Royal Society B: Biological Sciences.* 2011;278(1717):2429-2436.
48. Reece SE, Prior KF, Mideo N. The life and times of parasites: Rhythms in strategies for within-host survival and between-host transmission. *Journal of Biological Rhythms.* 2017;32(6):516-533.
49. Aidan JOD, Petra S, Harriet GM, Sarah ER. Fitness costs of disrupting circadian rhythms in malaria parasites. *Proceedings: Biological Sciences.* 2011(1717):2429.
50. Su Y, Ruan S, Wei J. Periodicity and synchronization in blood-stage malaria infection. *Journal Of Mathematical Biology.* 2011;63(3):557-574.
51. Farrow SN, Solari R, Willson TM. The importance of chronobiology to drug discovery. *Expert Opinion on Drug Discovery.* 2012;7(7):535-541.
52. Landau I, Caillard V, Beauté-Lafitte A, Chabaud A. Chronobiology and chronotherapy of malaria: investigations with murine malaria models. *Parassitologia (Roma).* 1993;35:55-57.

53. Joyner C, Moreno A, Meyer EVS, et al. Plasmodium cynomolgi infections in rhesus macaques display clinical and parasitological features pertinent to modelling vivax malaria pathology and relapse infections. *Malaria Journal.* 2016;15:1-18.
54. Moreno A, Cabrera-Mora M, Garcia A, et al. Plasmodium coatneyi in Rhesus Macaques Replicates the Multisystemic Dysfunction of Severe Malaria in Humans. *Infection and Immunity.* 2013;81(6):1889-1904.
55. Collins WE, Warren M, Sullivan JS, Galland GG. Plasmodium coatneyi: observations on periodicity, mosquito infection, and transmission to Macaca mulatta monkeys. 2001(3/4):101.
56. Pedregosa F, Varoquaux G, Gramfort A, et al. Scikit-learn: Machine Learning in Python. In:2012.

CHAPTER 4

MODELING THE INTERACTION BETWEEN THE MALARIA PARASITE AND HOST GLUCOSE CONCENTRATIONS[1]

---

[1]Jessica A. Brady and K. Melissa Hallow. To be submitted to *American Journal of Physiology*.

4.1 ABSTRACT

The malaria parasite cannot store energy and instead relies on host erythrocytic glucose as an energy source during the human blood stage. The exact mechanism for synchronization of the erythrocytic cycle bursting is unknown. Traditionally, this synchronization of erythrocyte bursting was thought to be related to light stimulus. A recent published study[1] showed that the erythrocytic cycle timing changes 12 hours based on nightly feeding times as opposed to daily feeding times; this suggests that glucose availability could be related to this synchronization. We hypothesize that erythrocytic bursting and parasite release could be related to exhaustion of glucose and consequently decreased erythrocytic adenosine triphosphate (ATP) levels. In order to investigate how the malaria life cycle synchronizes with the host's glucose concentration and metabolism, we constructed a model that incorporates plasma glucose and insulin dynamics, glucose transport into red blood cells, and erythrocytic glucose conversion to ATP. By modeling diurnal glucose concentrations and incorporating parasite dynamics, we aim to test our hypothesis mathematically and further investigate the relationship between erythrocytic glucose and parasite synchronization. A better understanding of the interaction between the host's erythrocytes glucose concentrations and the malaria parasite is needed to aid in the development of future treatment strategies to combat disease progression.

4.2 INTRODUCTION

An interesting relationship occurs between the malaria parasite and the host's red blood cell that it invades during the blood stage or erythrocytic cycle. Since erythrocytes do not contain mitochondria, they rely on glucose undergoing anaerobic glycolysis to obtain adenosine triphosphate (ATP). Similarly, the malaria parasite cannot store energy and relies on the host's intracellular glucose which it then metabolizes for energy. Upon entrance into the red blood cell (RBC), the parasite, forms a parasitophorous vacuole to contain itself within the cell. While the malaria parasite is in this vacuole, it undergoes asexual multiplication. The parasite changes the red blood cell's typical discoid shape, plasma membrane permeability, rigidity of the membrane, and other characteristics[2].

Mathematical modeling has been used to characterize malaria infection in multiple contexts. Epidemiological models[3,4] have been used to understand transmission of disease. Models describing within-host dynamics and RBC population dynamics have been used to better understand disease progression[5-7]. Parasite access and metabolism of glucose has also been quantified[8,9].

The majority of the infected red blood cells (iRBC) burst and release the parasites, called merozoites at this stage, into the blood every 24, 48, or 72 hours depending on the species/strain of *Plasmodium*[10]. Once in the red blood cell, parasites undergo asexual multiplication, erythrocytic schizogony, which includes the cycle of merozoites infecting RBCs, maturation of trophozoites, and maturation and bursting of schizonts which releases merozoites into the blood. This bursting is mostly synchronized to the same time of day in the infected red blood cells, but the underlying mechanism is not fully known[10]. Traditionally, this synchronization of erythrocyte bursting was thought to be related to light stimulus.

A recent study by Prior et al.[1] showed that the bursting time changed 12 hours between two populations of mice based on whether they were light or dark fed (the light-dark cycle was the same for both groups). This was surprising because it suggested that glucose availability may play a significant role in this synchronization.

We know that the malaria parasite utilizes glucose for glycolysis and thus energy, but the relationship between parasite growth and glucose availability has not been quantified. Additionally, we do not know how the erythrocytic glucose concentration and consequently ATP levels may change as the parasite grows. If the RBC is depleted of glucose by the parasite, then ATP levels would be expected to drop as well. ATP is needed for the cell to maintain the integrity of its plasma membrane. Thus, if ATP is depleted due to the parasite's presence, then this could be an important factor in the timing of RBC bursting and release of the parasites. The time of meal administration and other unknown factors could affect these dynamics as well. Since these processes can be difficult to measure experimentally *in vivo*, mathematical modeling may allow us to address some of these knowledge gaps. Modeling could inform future experiments needed to better understand these interactions and further test hypotheses related to the relationship of host glucose concentrations and parasite dynamics.

To better understand the relationship between the parasite and host RBC through modeling we need to characterize the processes that affect RBC glucose concentrations and the corresponding current existing models. First, we need to describe plasma glucose and insulin dynamics to find the plasma glucose concentrations that would determine the extracellular RBC conditions. Meals affect plasma glucose and consequently erythrocytic glucose concentrations and should be simulated to mimic human host conditions. A well-established model by Jauslin et al.[11-13] describes plasma glucose and insulin dynamics and simulates meals through an absorption

compartment. However, it does not specifically model RBC metabolism. Glucose transporter 1 (GLUT1) transports glucose between the cell and blood. There are multiple transport models[14,15] that describe this process. However, they do not incorporate the processes affecting extracellular conditions and intracellular processes such as the glucose and insulin feedback mechanism and glycolysis. Once glucose is transported into the RBC, about 90% undergoes glycolysis and 10% goes to the pentose pathway[16]. There are multiple in-depth models of glycolysis and ATP generation that include feedback mechanisms[17-20]. However, these models characterize many of the species involved and are beyond the scope of this research. We need to have glycolysis expressed in a way that can then inform ATP production since the net molar yield of ATP from glucose is 1:2. The ATP concentration can be used to estimate a time of bursting once the levels drop below a lysis threshold as described later.

To our knowledge, there are not any models that relate plasma glucose dynamics with RBC glucose dynamics, rates of glycolysis, and ATP generation. Furthermore, no model has characterized the effect of the malaria parasite dynamics on intracellular glucose and ATP.

To investigate the relationship between intracellular erythrocytic glucose availability and the malaria parasite, we constructed a mathematical model including plasma and erythrocytic glucose concentrations and parasite dynamics. We hypothesize that parasite bursting and parasite release could be due to glucose and thus ATP depletion in the red blood cells. We simulate steady state healthy erythrocytic conditions and then introduce the effect of the parasite on an erythrocyte to test our hypothesis. Since the exact relationship between glucose availability and parasite growth is unknown, we simulated several possible cases for this relationship with both day and night feeding to see how this might affect the time of bursting.

4.3 METHODS

4.3.1 Overall Model Description

In order to characterize the interaction between the malaria parasite and erythrocytic glucose concentrations, we first described glucose transport between the plasma to the red blood cell, as well as glucose utilization under healthy red blood cell conditions. A published mathematical model of glucose and insulin dynamics[11-13] and a published model of glucose transport through the cell membrane[14] were utilized, linked, and extended to describe the glucose concentrations in red blood cells. All differential equations were modeled in mM/min and corresponding parameter descriptions and values can be found in Table 4.1.

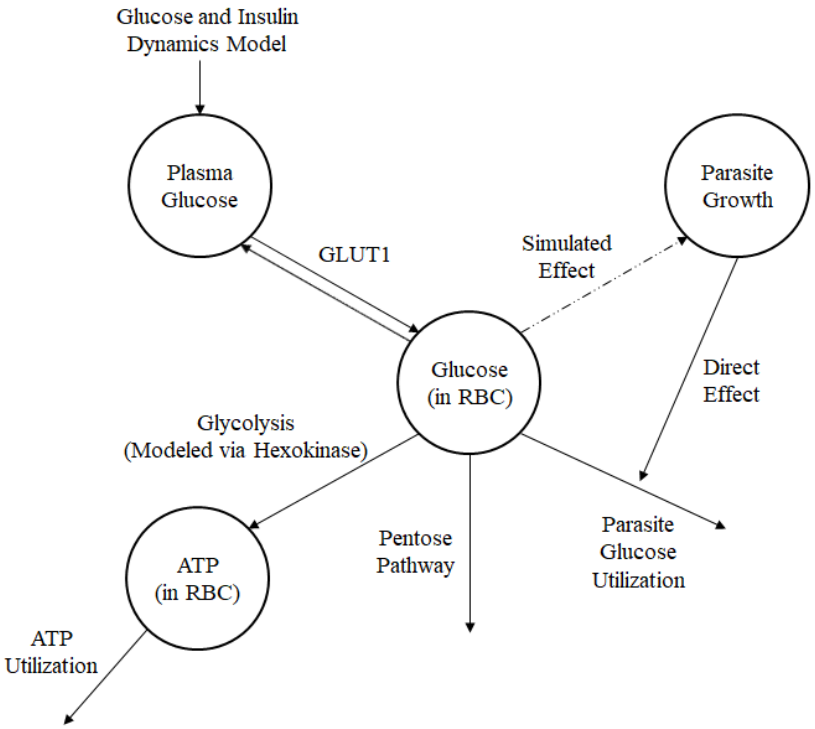

Figure 4.1. Model Schematic. Glucose and insulin dynamics model from Jauslin et al[11-13] was used to model plasma glucose concentrations with adaptations to include red blood cell glucose utilization. Glucose transporter 1, GLUT1, transports glucose between the plasma and inside the red blood cell. A glucose transport model from Alonso et al[14] was adapted to describe this process. Glycolysis was simplified and modeled via hexokinase with the assumption that once glucose entered this pathway, it would complete glycolysis. Parasite growth was modeled using

multiple growth equations to test different hypotheses. Multiple scenarios for parasite growth dependence upon erythrocytic glucose concentrations were simulated.

4.3.2 Plasma Glucose, Glucose Transport, and Intracellular Erythrocyte

Plasma glucose and insulin dynamics were described using a published model[11-13] to represent the plasma glucose available to red blood cells. The parameters describing a healthy individual's glucose and insulin dynamics were taken from Brady et al[21]. The rate of change in the plasma glucose [GLU_{Plasma}] from this model still included the sum of the glucose absorption rate (ABSG), endogenous glucose production rate (G_{PRO}), glucose elimination rate (G_{ELI}), and glucose distribution rate (G_{DIS}) where V_G represents the volume of distribution of glucose. Since red blood cells are responsible for roughly 10% of glucose metabolism in the body[16], total glucose elimination G_{ELI} is divided into two terms – $G_{ELI\text{-}non\text{-}RBC}$, and a new term describing glucose utilization by RBC. At baseline, $G_{ELI\text{-}non\text{-}RBC}$ is set to 90% of the baseline total G_{ELI}, while the RBC glucose elimination term is constrained such that it equals 10% of baseline G_{ELI} (described later). Thus, the remaining additions to the plasma glucose equation reflected the transport of glucose across the red blood cell membrane in order to incorporate red blood cell utilization of glucose. The details of the model of transport of glucose across the red blood cell membrane are described in the next section. From this model, the rate of glucose movement into and out of the red blood cell is calculated per liter of RBC ($GLU_{LeavingRBC}$ and $GLU_{EnteringRBC}$). Net glucose entering all red blood cells is calculated as the difference of these rates, multiplied by total volume of red blood cells, 2 L, which is 40% of the average volume of blood in humans, 5 L. At steady state, this amounts to about 10% of total glucose elimination from the body which was consistent with what we would expect for red blood cell glucose utilization.

$$\frac{d[GLU_{Plasma}]}{dt} = \left(\frac{1}{V_G}\right) * \left(ABSG + G_{PRO} - G_{ELI-non-RBC} - G_{DIS} + V_{RBC} * \left(GLU_{LeavingRBC} - GLU_{EnteringRBC}\right)\right) \quad \text{(Eq. 4.1)}$$

Glucose transporter 1 [GLUT1] transports glucose across the red blood cell membrane in both directions and is an asymmetric carrier. A published model[14] describing the transporter, its conformations, and changes in internal and external glucose concentrations was utilized and extended to model the relationship between plasma glucose and intracellular erythrocytic glucose concentrations [GLU_{RBC}]. [GLUT1] can be described as facing internally where the glucose-binding site faces the inside of the cell (I) or externally where the glucose-binding site is visible on the outer surface of the RBCs plasma membrane (E). [GLUT1] was denoted as either bound (B) or unbound (U) with respect to glucose. Thus, there are a combination of states for the transporter for us to model.

$$\frac{d[GLUT1_{E_U}]}{dt} = k_4 * [GLUT1_{I_U}] + \ k_{-1} * [GLUT1_{E_B}] - [GLUT1_{E_U}] * (k_1 * [GLU_{Plasma}] + k_{-4}) \quad \text{(Eq. 4.2)}$$

$$\frac{d[GLUT1_{E_B}]}{dt} = k_1 * [GLUT1_{E_U}] * [GLU_{Plasma}] + \ k_{-2} * [GLUT1_{I_B}] - [GLUT1_{E_B}] * (k_{-1} + k_2) \quad \text{(Eq. 4.3)}$$

$$\frac{d[GLUT1_{I_B}]}{dt} = k_2 * [GLUT1_{E_B}] + \ k_{-3} * [GLUT1_{I_U}] * [GLU_{RBC}] - [GLUT1_{I_B}] * (k_{-2} + k_3) \quad \text{(Eq. 4.4)}$$

$$\frac{d[GLUT1_{I_U}]}{dt} = k_3 * [GLUT1_{I_B}] + \ k_{-4} * [GLUT1_{E_U}] - [\ GLUT1_{I_U}] * (k_{-3} * [GLU_{RBC}] + k_{-4}) \quad \text{(Eq. 4.5)}$$

Ultimately, the glucose transport equations allowed us to quantify changes in the rates of glucose leaving the red blood cell ($GLU_{LeavingRBC}$) and entering the red blood cell ($GLU_{EnteringRBC}$).

$$GLU_{LeavingRBC} = k_{-1} * [GLUT1_{E_B}] - k_1 * [GLUT1_{E_U}] * [GLU_{Plasma}] \quad \text{(Eq. 4.6)}$$

$$GLU_{EnteringRBC} = k_3 * [GLUT1_{I_B}] - k_{-3} * [GLUT1_{I_U}] * [GLU_{RBC}] \quad \text{(Eq. 4.7)}$$

As seen in Equations 4.1 and 4.10, the net glucose transport is the difference between these values where the positive or negative reference is either the plasma or the red blood cell.

The published model for glucose transport[14] did not model plasma glucose interactions or internal metabolic processes that utilized glucose. To quantify changes in [GLU_{RBC}], glycolysis was modeled by incorporating kinetics of the first enzyme that catalyzes glycolysis, hexokinase.

Hexokinase can either be bound (B) or unbound (U) with respect to glucose. We assumed hexokinase is saturated at steady state under normal physiological conditions. Although there are many complex steps and feedback mechanisms for glycolysis in the red blood cell, we assumed that once glucose was bound to hexokinase, the entire glycolysis pathway would be completed. Hexokinase is the first rate limiting step in glycolysis and has the slowest *in vitro* enzymatic activity compared to all of the other glycolytic enzymes[16,22]. Hexokinase affinity for glucose[23], K_m, has been measured experimentally and was used to find values for the parameters $k_{1_{HK}}$ and $k_{-1_{HK}}$, as described in Table 4.1.

$$\frac{d[HK_U]}{dt} = -k_{1_{HK}} * [HK_U] * [GLU_{RBC}] + [HK_B] * (k_{-1_{HK}} + k_{2_{HK}}) \quad \text{(Eq. 4.8)}$$

$$\frac{d[HK_B]}{dt} = k_{1_{HK}} * [HK_U] * [GLU_{RBC}] - [HK_B] * (k_{-1_{HK}} + k_{2_{HK}}) \quad \text{(Eq. 4.9)}$$

Combining the net glucose transported inside the red blood cell, glycolysis modeled by hexokinase, and the pentose pathway which accounts for 10% of glucose utilization by RBCs, we obtained the expression for intracellular glucose, $[GLU_{RBC}]$.

$$\frac{d[GLU_{RBC}]}{dt} = (k_3 * [GLUT1_{I_B}] - k_{-3} * [GLUT1_{I_U}] * [GLU_{RBC}]) - (k_{-1} * [GLUT1_{E_B}] - k_1 * [GLUT1_{E_U}] * [GLU_{Plasma}]) - k_{1_{HK}} * [HK_U] * [GLU_{RBC}] + k_{-1_{HK}} * [HK_B] - 0.10 * \frac{G_{ELI-RBC}}{V_G} \quad \text{(Eq. 4.10)}$$

We assume that once glucose is bound to hexokinase, it completes the rest of the glycolysis pathway, with a net yield of 2 moles of ATP per mole of glucose. Thus, the rate of ATP generation was 2 times the rate of glycolysis. ATP utilization was set to equal this rate at steady state.

$$\frac{d[ATP_{RBC}]}{dt} = 2 * (k_{2_{HK}} * [HK_B]) - ATP_{Utilization} \quad \text{(Eq. 4.11)}$$

4.3.3 Parasitic Growth and Corresponding Glucose Utilization

When the *Plasmodium* parasite enters a red blood cell, it relies on intracellular glucose for energy as it matures. Thus, glucose in the infected red blood cell (GLU_{iRBC}) also changes as a function of the schizont maturity. In our model we focused on describing the early stages of infection with a small enough number of infected red blood cells such that plasma glucose was not affected by the infected red blood cells yet. However, we know that an infected red blood cell can take in up to 100-fold more glucose than an uninfected red blood cell during late stage of schizont maturity[8,24]. We modeled schizont maturity or parasite growth as the number of merozoites that would be released from the red blood cell if it burst at that moment. Since the number of merozoites at the time of bursting is 10 on average[25], we estimated that the host's erythrocytic glucose would be depleted by a factor of ten times the parasite maturity being modeled times the typical red blood cell glucose utilization. Thus, parasite glucose utilization in mM/min is $10 * Parasites * GLU_{RBCUtilization}$ where the parasites per RBC were evaluated in three different cases to be described in the next section.

$$\frac{d[GLU_{iRBC}]}{dt} = (k_3 * [GLUT1_{I_B}] - \ k_{-3} * [GLUT1_{I_U}] * [GLU_{RBC}]) - (k_{-1} * [GLUT1_{E_B}] - k_1 * [GLUT1_{E_U}] * [GLU_{Plasma}]) - \ k_{1_{HK}} * [HK_U] * [GLU_{RBC}] + k_{-1_{HK}} * [HK_B] - 0.10 * \frac{G_{ELI-RBC}}{V_G} - 10 * Parasites * GLU_{RBCUtilization} \quad \text{(Eq. 4.12)}$$

Table 4.1. Parameters Values for Healthy Red Blood Cell Conditions

Parameter	Description	Value	Units
k_1	$GLUT1_{E/U}$ binds to external glucose and becomes $GLUT1_{E/B}$	6.00×10^4	$mM^{-1}\ min^{-1}$
k_{-1}	$GLUT1_{E/B}$ releases glucose externally and becomes $GLUT1_{E/U}$	3.12×10^5	min^{-1}
k_2	$GLUT1_{E/B}$ changes conformation to $GLUT1_{I/B}$	6.00×10^4	min^{-1}
k_{-2}	$GLUT1_{I/B}$ changes conformation to $GLUT1_{E/B}$	6.00×10^4	min^{-1}
k_3	$GLUT1_{I/B}$ releases glucose internally and becomes $GLUT1_{I/U}$	3.12×10^5	min^{-1}
k_{-3}	$GLUT1_{I/U}$ binds to internal glucose and becomes $GLUT1_{I/B}$	6.00×10^4	$mM^{-1}\ min^{-1}$
k_4	$GLUT1_{I/U}$ changes conformation to $GLUT1_{E/U}$	6.00×10^4	min^{-1}
k_{-4}	$GLUT1_{E/U}$ changes conformation to $GLUT1_{I/U}$	6.00×10^4	min^{-1}
$k_{1\ HK}$	Hexokinase binds to glucose to begin glycolysis. $k_{1_{HK}} = (k_{-1_{HK}} + k_{2_{HK}})/K_m$	1.38×10^6	min^{-1}
$k_{-1\ HK}$	Hexokinase becomes unbound. Value was determined using steady-state concentrations.	5.70×10^4	min^{-1}
$k_{2\ HK}$	Hexokinase phosphorylates glucose to glucose-6-phosphate. Calculated by dividing normal hexokinase activity determined by steady state conditions, 1.64×10^{-1}, by initial condition for HK_B.	2.57×10^4	min^{-1}
K_m	Hexokinase affinity for glucose. Value within experimental range reported[23]. Used to find other Hexokinase parameters.	6.00×10^{-2}	mmol
$GLU_{RBCUtilization}$	Steady State Glucose Utilization by Healthy RBC	3.80×10^{-1}	mM/min

4.3.4 Analysis Approach

We simulated several scenarios for the parasite's growth to investigate its dependence upon erythrocytic glucose concentrations and when ATP levels drop below the lysis threshold indicating time of bursting as described later. Since the parasite growth dependence upon glucose

is not fully understood, we simulated several cases for this relationship to investigate the effect on ATP concentrations.

Case 1: We assumed that the parasite maturity depends upon the glucose concentrations within the red blood cell. If the erythrocytic glucose concentration in the infected red blood cell GLU_{iRBC} drops below typical steady state concentrations (GLU_{SS}) then the growth is slowed, but if the concentration surpasses GLU_{SS} then the growth will increase. Under these conditions we simulated 2 types of growth: Case 1A represented exponential growth for the parasite (Eq. 4.13) and Case 1B represented logistic growth for the parasite (Eq. 4.14). Exponential and logistic growth are commonly used in population simulations. The parameter K in the logistic growth equation is defined as the carrying capacity of the environment. In this case it is equal to 10 since the average number of merozoites release upon bursting is 10 for *Plasmodium*[25]. Parameter descriptions and values can be found in Table 4.2.

$$\frac{d(Parasites)}{dt} = \frac{GLU_{iRBC}}{GLU_{SS}} * k_{ExpGrowth} * Parasites \quad \text{(Eq. 4.13)}$$

$$\frac{d(Parasites)}{dt} = \frac{GLU_{iRBC}}{GLU_{SS}} * r_{Logistic} * Parasites \left(1 - \left(\frac{Parasites}{K}\right)\right) \quad \text{(Eq. 4.14)}$$

Case 2: We assumed parasite growth was affected when glucose concentrations, $GLU_{iRBC,}$ dropped below baseline concentrations but was not affected by greater glucose concentrations in the red blood cell. Case 2A represented exponential growth for the parasite (Eq. 4.15) and Case 2B represented logistic growth for the parasite (Eq. 4.16). Parameter descriptions and values can be found in Table 4.2.

$$\frac{d(Parasites)}{dt} = \min\left(1, \frac{GLU_{iRBC}}{GLU_{SS}}\right) * k_{ExpGrowth} * Parasites \quad \text{(Eq. 4.15)}$$

$$\frac{d(Parasites)}{dt} = \min\left(1, \frac{GLU_{iRBC}}{GLU_{SS}}\right) * r_{Logistic} * Parasites \left(1 - \left(\frac{Parasites}{K}\right)\right) \quad \text{(Eq. 4.16)}$$

Case 3: We assumed parasite growth was not dependent upon glucose. Case 3A represented exponential growth for the parasite (Eq. 4.17) and Case 3B represented logistic growth for the parasite (Eq. 4.18). Parameter descriptions and values can be found in Table 4.2.

$$\frac{d(Parasites)}{dt} = k_{ExpGrowth} * Parasites \quad \text{(Eq. 4.17)}$$

$$\frac{d(Parasites)}{dt} = r_{Logistic} * Parasites \left(1 - \left(\frac{Parasites}{K}\right)\right) \quad \text{(Eq. 4.18)}$$

Table 4.2. Parameters Values for Infection Simulations. The parameters are used to simulate different cases as described in Equations 4.13 - 4.18.

Parameter	Description	Value	Units
$k_{ExpGrowth}$	Exponential growth constant	Cases 1, 2: 2.00×10^{-3} Case 3: 1.6×10^{-3}	
GLU_{SS}	Steady state glucose concentration	5.20×10^{1}	mM
K	Carrying capacity for logistic growth for parasite	1.00×10^{1}	Parasite Count per RBC
$r_{Logistic}$	Rate in logistic growth model representing the proportional increase of the parasites per unit of time.	5.00×10^{-3}	min^{-1}

4.4 RESULTS

We sought to model the interaction between the malaria parasite and erythrocytic glucose concentrations to test our hypotheses that infected red blood cells burst based on glucose and thus ATP deprivation. Figure 4.2 illustrates the steady state concentrations for plasma and erythrocytic glucose, as well as other key factors in the red blood cell that affect erythrocytic glucose concentrations. We then simulated a meal of about 100 g carbohydrates being given 3 times per day, Figure 4.3.

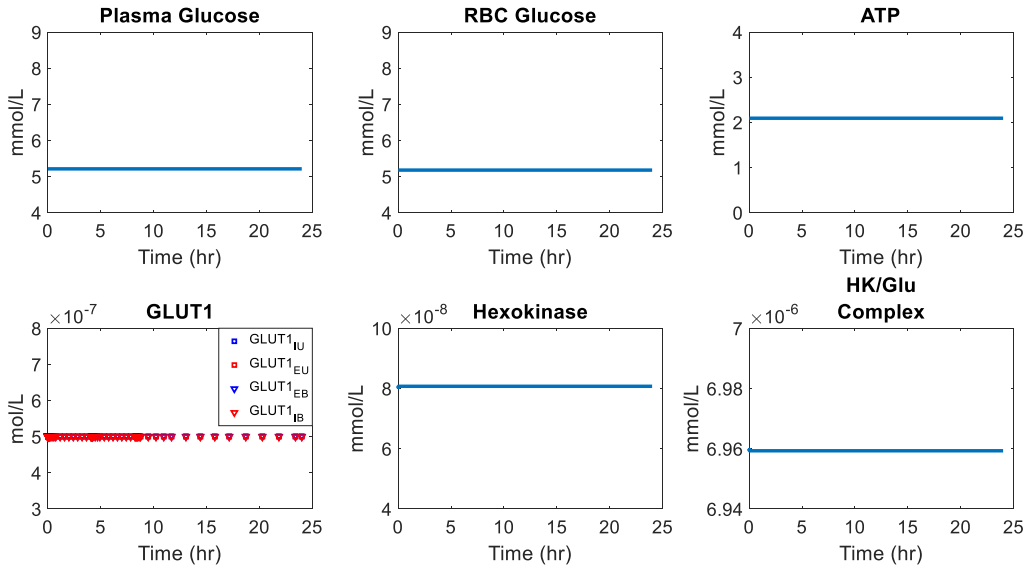

Figure 4.2. Healthy RBC Conditions at Steady State. All concentrations are in the red blood cell except for plasma glucose. GLUT1 conformations are represented as either bound or unbound and facing either internally or externally with respect to the red blood cell.

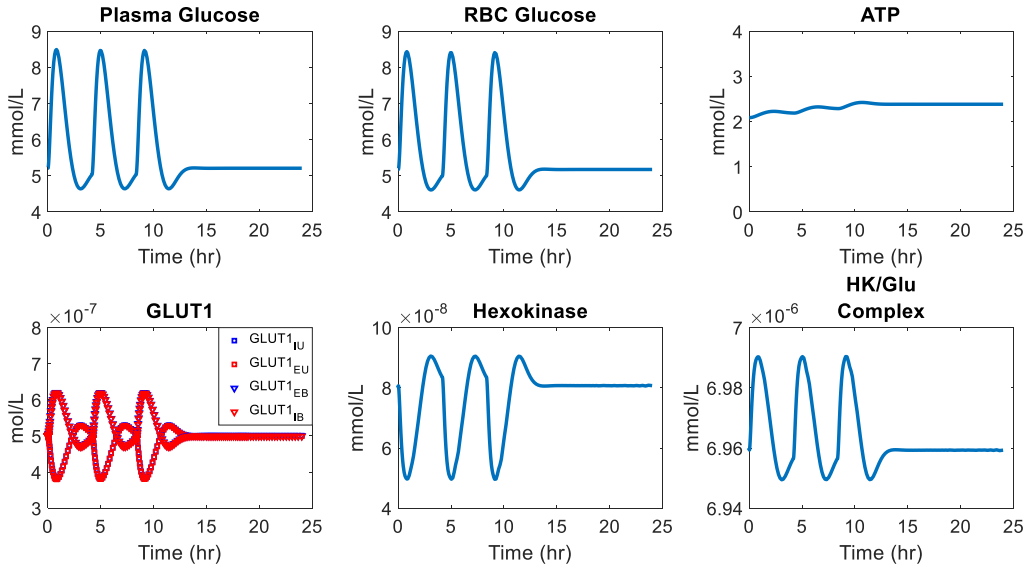

Figure 4.3. Healthy RBC Conditions for Simulation of 3 Standard Meals. Each meal contained approximately 100 g carbohydrates.

The parasite effect was then introduced and adjusted to simulate different scenarios. Case 1 assumed that the parasite growth was affected by glucose concentration, Eq. 4.13 and 4.14, such that the parasite growth rate increased when erythrocytic glucose was above baseline glucose concentration and decreased when below baseline. The simulation for night and day feeding for both exponential and logistic growth of the parasites can be seen in Figure 4.4. For all simulations, glucose and ATP depletion in the infected cell was evident. Here we estimated the time of RBC bursting as the time when intracellular ATP concentrations dropped below a lysis threshold, defined as 25% of baseline ATP concentrations which has been reported as the threshold between apoptosis and necrosis for endothelial cells[26]. The night feeding time simulation showed a slight delay in the time of bursting for the exponential growth conditions as compared to the day feeding times, Figure 4.4A,B. This is what we would expect since the greatest parasite glucose utilization occurred in the second half of the day and thus meals during this time minimized glucose depletion unlike the simulation for day feeding times when additional glucose was not available during peak glucose utilization. For the night feeding time simulation with exponential parasite growth, the RBC burst close to 24 hours whereas the day feeding time simulation burst a few hours earlier. For the logistic growth simulations, Figure 4.4C,D, both night and day feeding times resulted in similar bursting times, closer to 18 hours instead.

A

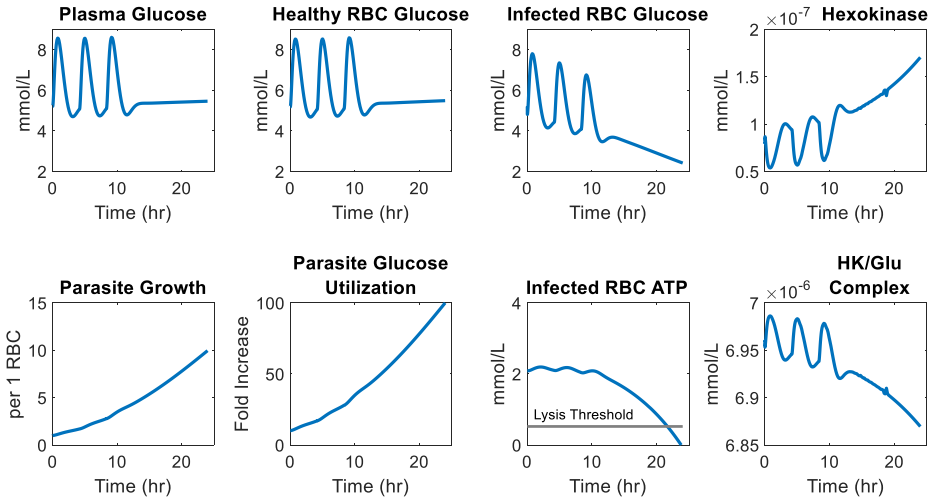
Plasma Glucose
Healthy RBC Glucose
Infected RBC Glucose
Hexokinase
mmol/L
Time (hr)
Parasite Growth
per 1 RBC
Parasite Glucose Utilization
Fold Increase
Infected RBC ATP
Lysis Threshold
HK/Glu Complex

B

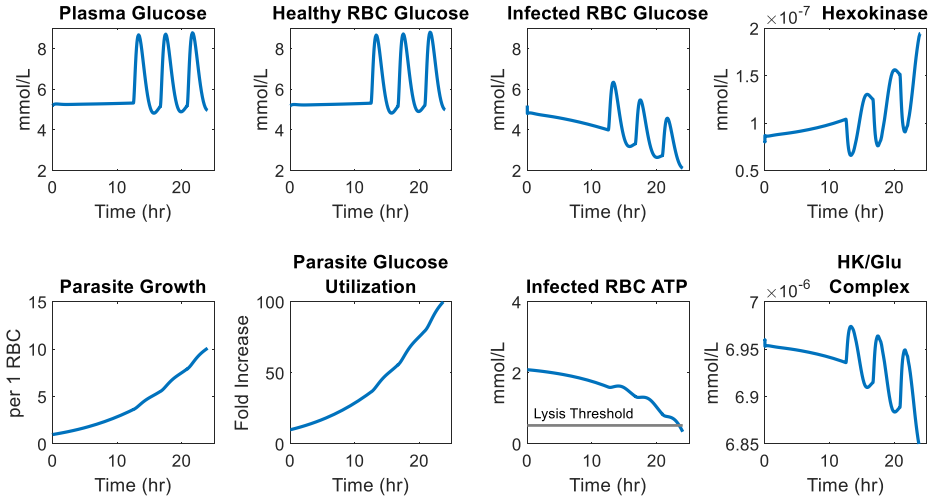
Plasma Glucose
Healthy RBC Glucose
Infected RBC Glucose
Hexokinase
mmol/L
Time (hr)
Parasite Growth
per 1 RBC
Parasite Glucose Utilization
Fold Increase
Infected RBC ATP
Lysis Threshold
HK/Glu Complex

C

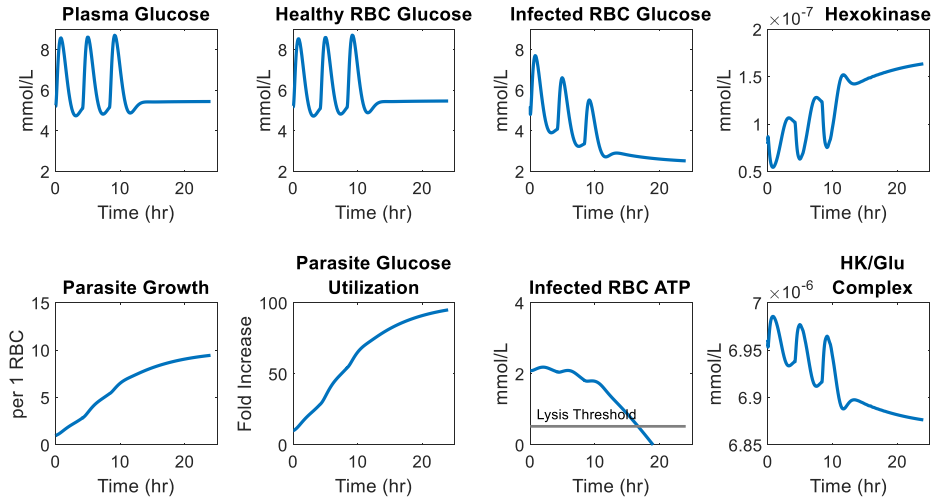

D

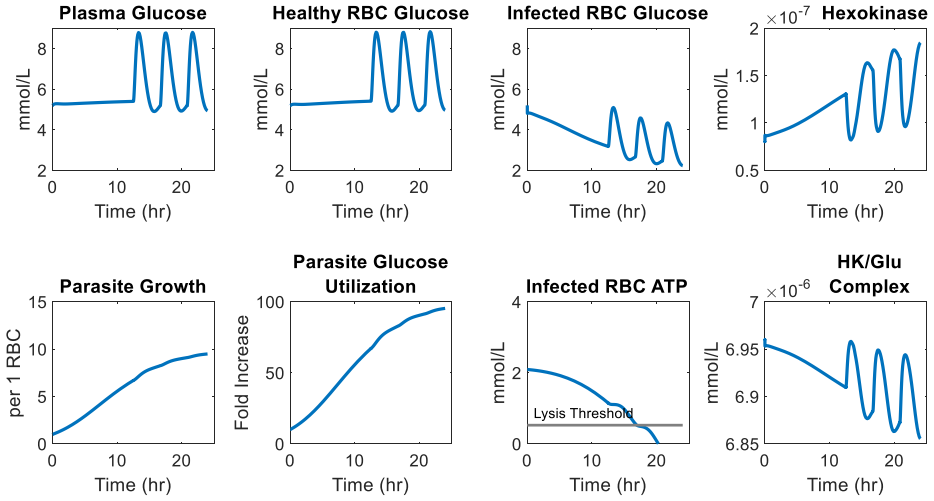

Figure 4.4. Healthy RBC Conditions vs Infected RBC Conditions for Case 1. Assumption: parasite growth is constantly affected by changes in erythrocytic glucose concentrations. Both exponential (**A,B**) and logistic (**C,D**) growth for the parasite were simulated. Meals were simulated during the day (**A,C**) and at night (**B,D**). The parasite glucose utilization is represented as a fold increase of parasite glucose utilization compared to healthy red blood cell utilization.

For Case 2, parasite growth was only affected when the erythrocytic glucose concentrations dropped below baseline, Eq. 4.14 and 4.15. The difference in time of bursting

between the night and day simulations in Figure 4.5A,B for exponential growth were more similar as compared to the difference for Case 1 for exponential growth day and night feeding simulations. This was expected since the feeding time or the time when glucose concentrations exceeded baseline should not affect parasite growth in this case. However, the period of time for glucose below baseline was slightly less for the night feeding simulation and hence minorly delayed the time of bursting. The logistic parasite growth simulations for Case 2, Figure 4.5C,D, had a closer time of bursting as opposed to the exponential growth simulations. In addition, the bursting for the logistic growth simulations were closer to 18 hours rather than 24 hours.

A

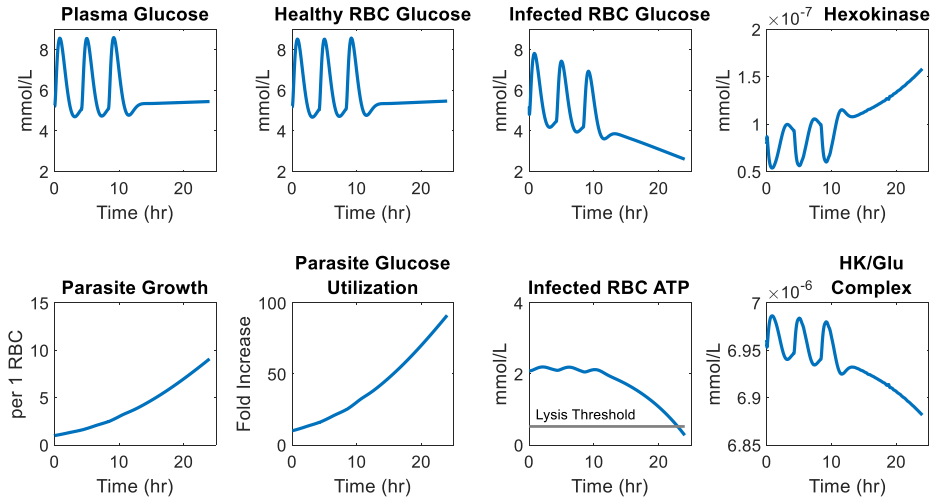
Plasma Glucose
Healthy RBC Glucose
Infected RBC Glucose
Hexokinase
Parasite Growth
Parasite Glucose Utilization
Infected RBC ATP
HK/Glu Complex
mmol/L
per 1 RBC
Fold Increase
Time (hr)
Lysis Threshold

B

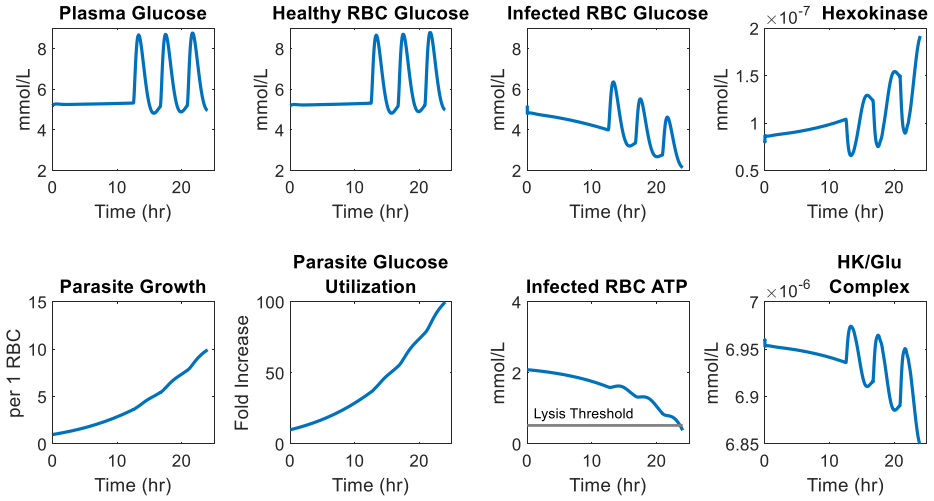
Plasma Glucose
Healthy RBC Glucose
Infected RBC Glucose
Hexokinase
Parasite Growth
Parasite Glucose Utilization
Infected RBC ATP
HK/Glu Complex
mmol/L
per 1 RBC
Fold Increase
Time (hr)
Lysis Threshold

C

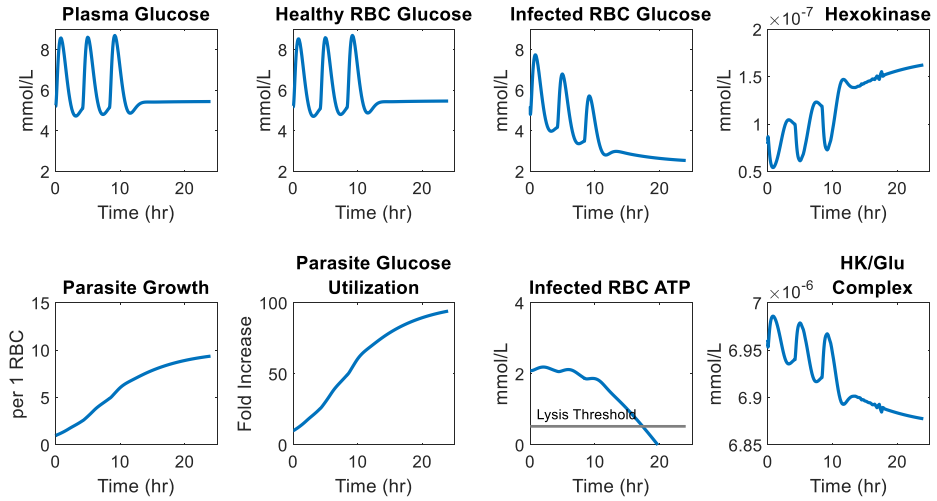

D

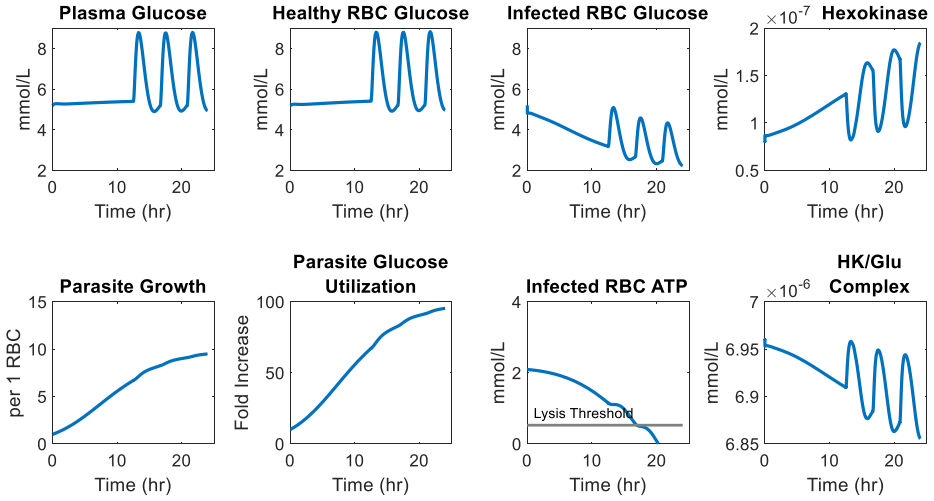

Figure 4.5. Healthy RBC Conditions vs Infected RBC Conditions for Case 2. Assumption: parasite growth is only affected when erythrocytic glucose concentrations drop below baseline. Both exponential (**A,B**) and logistic (**C,D**) growth for the parasite were simulated. Meals were simulated during the day (**A,C**) and at night (**B,D**). The parasite glucose utilization is represented as a fold increase of parasite glucose utilization compared to healthy red blood cell utilization.

For Case 3, parasite growth was independent of glucose concentrations. Thus, the parasite growth and parasite glucose utilization kept the traditional exponential (Figure 4.6A,B) or logistic growth (Figure 4.6C,D) curve shapes regardless of day or night feeding time simulations. Both exponential and logistic growth simulations reach 100-fold increase for parasite glucose utilization compared to an uninfected RBC. However, the burst times for the exponential growth simulations reach approximately 24 hours whereas the logistic growth simulations burst times are closer to 18 hours.

A

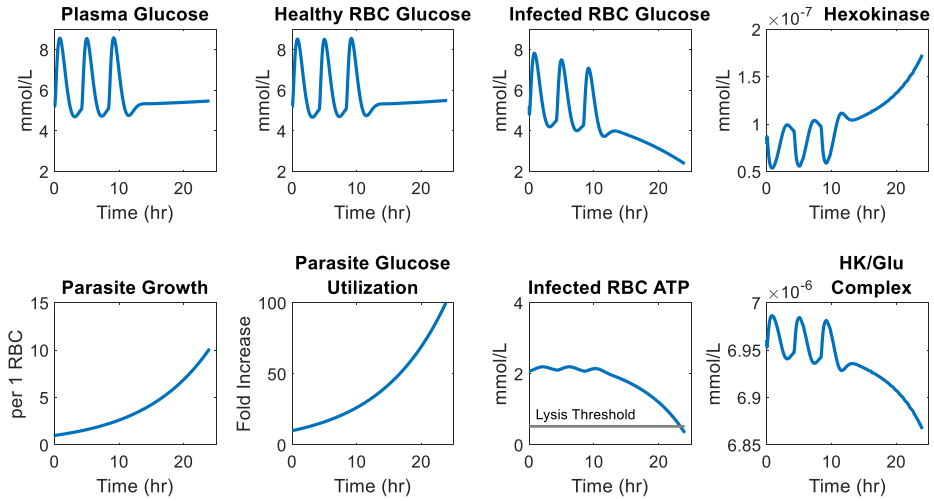
Plasma Glucose
Healthy RBC Glucose
Infected RBC Glucose
Hexokinase
mmol/L
Time (hr)
Parasite Growth
per 1 RBC
Parasite Glucose Utilization
Fold Increase
Infected RBC ATP
Lysis Threshold
HK/Glu Complex

B

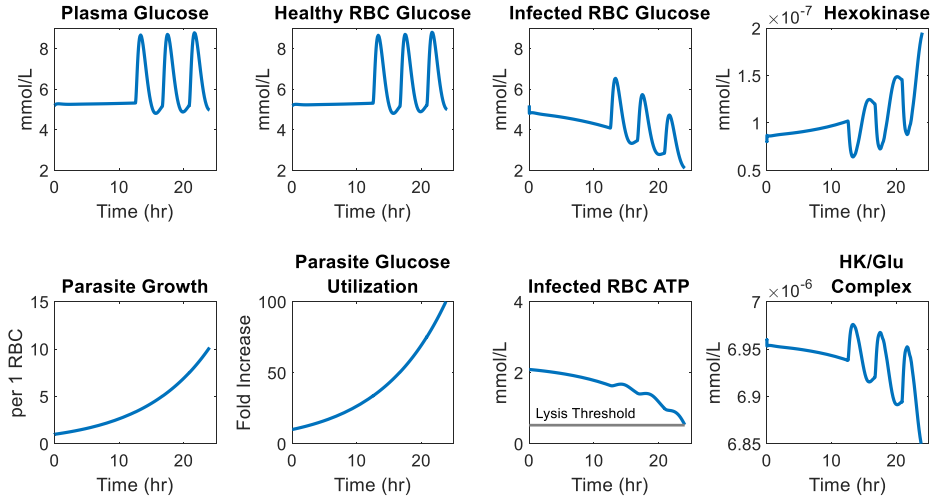
Plasma Glucose
Healthy RBC Glucose
Infected RBC Glucose
Hexokinase
mmol/L
Time (hr)
Parasite Growth
per 1 RBC
Parasite Glucose Utilization
Fold Increase
Infected RBC ATP
Lysis Threshold
HK/Glu Complex

C

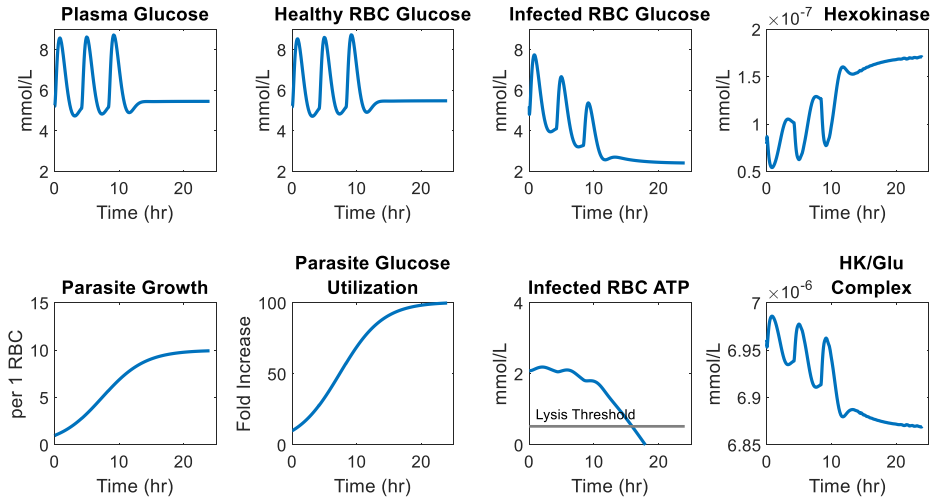

D

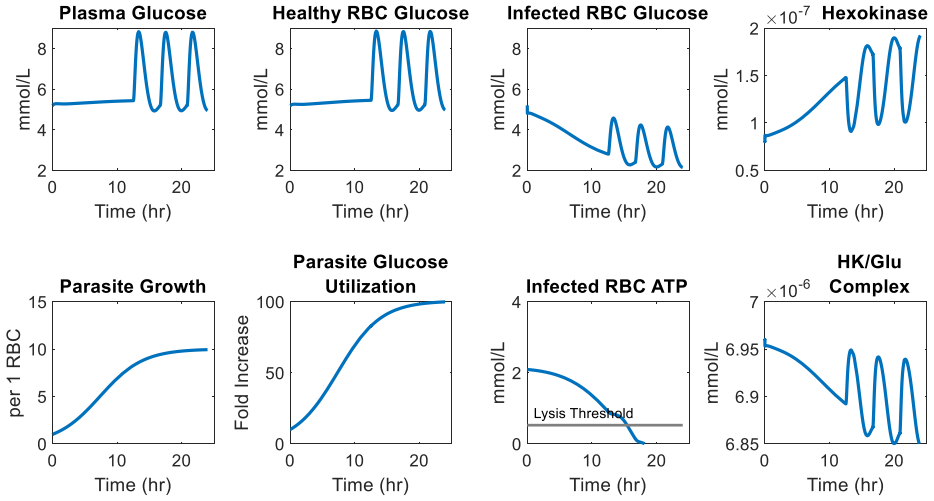

Figure 4.6. Healthy RBC Conditions vs Infected RBC Conditions for Case 3. Assumption: parasite growth is independent of glucose concentrations. Both exponential (**A,B**) and logistic (**C,D**) growth for the parasite were simulated. Meals were simulated during the day (**A,C**) and at night (**B,D**). The parasite glucose utilization is represented as a fold increase of parasite glucose utilization compared to healthy red blood cell utilization.

ATP concentrations and time of bursting were sensitive to several parameters, primarily the ones involved in modeling glycolysis. The parameter k_{2HK} was used to compute additional hexokinase rate parameter, k_{1HK}, and thus glycolysis rates and ATP production. Figure 4.7 illustrates how different values of k_{2HK} affect time of bursting due to ATP depletion for multiple cases and growth simulations for the parasite. In several cases, the ATP depletion does not reach the lysis threshold within 24 hours. For exponential growth simulations, the time of bursting was delayed through progression of cases as parasite growth dependence upon glucose concentrations waned.

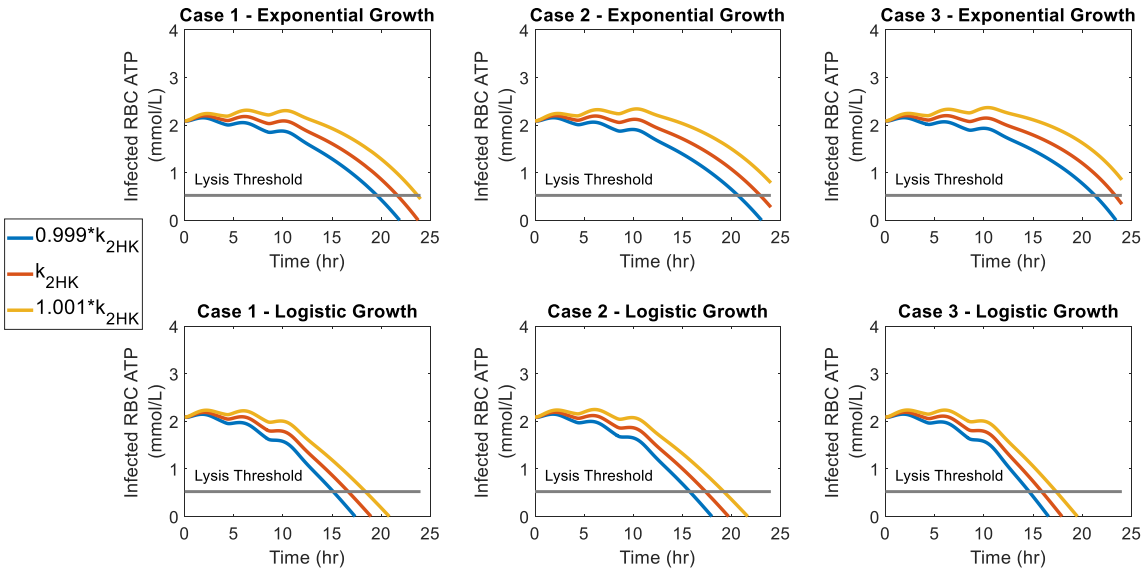

Figure 4.7. ATP Concentrations in Infected RBC with Variability in k_{2HK}. Simulations for day feeding in infected RBC based upon different case assumptions and growth simulations.

4.5 DISCUSSION

This study quantified the erythrocytic glucose and ATP concentrations and corresponding changes due to parasite dynamics in order to estimate the time of bursting due to glucose and consequently ATP depletion. To our knowledge, this modeling and simulation combination is

novel. The simulation cases for parasite growth dependence upon glucose showed that Case 1's assumption resulted in the greatest difference, although small, between the time of bursting for night vs day fed simulations. This would suggest that the actual parasite's growth could be influenced by erythrocytic glucose conditions whether they are above or below baseline since the Prior et al[1]. study showed a change in bursting time with different feeding times. However, the study showed that the change in burst time did not happen overnight once the feeding times changed. It was not until approximately the 5th day that this change occurred. However, for all cases we saw ATP depletion and thus RBC bursting around 18-24 hours.

The model did not take into consideration several factors that would need to be addressed for modeling malaria infection and systemic glucose changes once parasitemia is increased later in the blood stage. The model assumed that the red blood cell was mature and not a reticulocyte. Reticulocytes are in circulation in the blood for about 1-2 days before maturation. Reticulocytes have different glycolytic characteristics[27] and although they typically comprise about 1% of total RBCs, this percentage would change due to erythropoietic responses during malaria infection[6,28,29]. Certain species of *Plasmodia* demonstrate a preference for invading reticulocytes[30]. Thus, modeling RBC population dynamics would be important for modeling overall glucose changes later in the blood stage of infection.

Extension of this model could incorporate existing osmotic pressure models[19] for lysis in *Plasmodium* infected RBCs[31] and include a *Plasmodium* glycolysis model[9] to further test the hypothesis that the depletion of glucose and thus ATP, results in the inability for the red blood cell to maintain its active transport channels resulting in osmotic pressure increase in the cell and lysis. Since the malaria parasite changes plasma membrane characteristics[2], we would need to incorporate these as well to have a comprehensive RBC lysis model with parasite dynamics.

Plasmodium falciparum hexose transporter (PfHT) inhibitors have recently been identified as possible anti-malarial drug targets[32-34]. If the parasites are deprived of glucose while in the RBC, their growth is inhibited. One obstacle for development of PfHT inhibitors is to specifically block PfHT and not host GLUT1. A recent study began identifying potential compounds that were high affinity, high selectivity inhibitors of PfHT[34]. Further work with our model could be done to quantify the effects of different PfHT inhibitors.

Our model simulations showed that exponential growth consistently reproduced bursting around 18-24 hours even with different parasite growth assumptions. These simulations could better inform future experiments. Glucose utilization by the parasite as a function of parasite maturity would be a valuable experiment to better inform hypotheses and even drug development for PfHT inhibitors.

4.6 REFERENCES

1. Prior KF, Veen DRvd, O'Donnell AJ, et al. Timing of host feeding drives rhythms in parasite replication. *PLoS Pathogens.* 2018;14(2):e1006900-e1006900.
2. Mohandas N, An X. Malaria and human red blood cells. *Medical microbiology and immunology.* 2012;201(4):593-598.
3. Siettos CI, Russo L. Mathematical modeling of infectious disease dynamics. *Virulence.* 2013;4(4):295-306.
4. Mandal S, Sarkar RR, Sinha S. Mathematical models of malaria - a review. *Malaria Journal.* 2011;10(1):202.
5. Fonseca LL, Alezi HS, Moreno A, Barnwell JW, Galinski MR, Voit EO. Quantifying the removal of red blood cells in Macaca mulatta during a Plasmodium coatneyi infection. *Malaria Journal.* 2016;15(1):410.
6. Fonseca LL, Voit EO. Comparison of mathematical frameworks for modeling erythropoiesis in the context of malaria infection. *Mathematical Biosciences.* 2015;270:224-236.
7. Yan Y, Adam B, Galinski M, C. Kissinger J, Moreno A, Gutierrez JB. Mathematical model of susceptibility, resistance, and resilience in the within-host dynamics between a Plasmodium parasite and the immune system. *Mathematical Biosciences.* 2015;270:213-223.
8. Kirk K, Horner HA, Kirk J. Glucose uptake in Plasmodium falciparum-infected erythrocytes is an equilibrative not an active process. *Molecular and Biochemical Parasitology.* 1996;82(2):195-205.
9. Penkler G, du Toit F, Adams W, et al. Construction and validation of a detailed kinetic model of glycolysis in Plasmodium falciparum. In. Vol 2822015:1481-1511.
10. Mideo N, Reece SE, Smith AL, Metcalf CJE. The Cinderella syndrome: why do malaria-infected cells burst at midnight? *Trends in Parasitology.* 2013;29(1):10-16.
11. Jauslin PM, Frey N, Karlsson MO. Modeling of 24-Hour Glucose and Insulin Profiles of Patients With Type 2 Diabetes. *The Journal of Clinical Pharmacology.* 2011;51(2):153-164.
12. Jauslin PM, Silber HE, Frey N, et al. An integrated glucose-insulin model to describe oral glucose tolerance test data in type 2 diabetics. *Journal of Clinical Pharmacology.* 2007(10):1244.
13. Silber HE, Jauslin PM, Frey N, Gieschke R, Simonsson USH, Karlsson MO. An Integrated Model for Glucose and Insulin Regulation in Healthy Volunteers and Type 2 Diabetic Patients Following Intravenous Glucose Provocations. *The Journal of Clinical Pharmacology.* 2007;47(9):1159-1171.
14. Alonso GL, González DA. In Silico Kinetic Study of the Glucose Transporter. *Journal of Biological Physics.* 2007;33(5-6):485.
15. Baker GF, Widdas WF. The asymmetry of the facilitated transfer system for hexoses in human red cells and the simple kinetics of a two component model. *The Journal of physiology.* 1973;231(1):143-165.
16. Baynes JW, Dominiczak MH. *Medical biochemistry.* Edinburgh : Saunders Elsevier, 2014. Fourth edition.; 2014.

17. du Preez FB, Conradie R, Penkler GP, Holm K, van Dooren FLJ, Snoep JL. A comparative analysis of kinetic models of erythrocyte glycolysis. *Journal of Theoretical Biology.* 2008;252(3):488-496.
18. Rapoport TA, Heinrich R. Mathematical analysis of multienzyme systems. I. Modelling of the glycolysis of human erythrocytes. *Biosystems.* 1975;7(1):120-129.
19. Brumen M, Heinrich R. A metabolic osmotic model of human erythrocytes. *Biosystems.* 1984;17(2):155-169.
20. Jamshidi N, Edwards JS, Fahland T, Church GM, Palsson BO. Dynamic simulation of the human red blood cell metabolic network. In. Great Britain: OXFORD UNIVERSITY PRESS; 2001:286.
21. Brady JA, Hallow KM. Model-Based Evaluation of Proximal Sodium Reabsorption Through SGLT2 in Health and Diabetes and the Effect of Inhibition With Canagliflozin. *Journal of Clinical Pharmacology.* 2018;58(3):377-385.
22. van Wijk R, van Solinge WW. The energy-less red blood cell is lost: erythrocyte enzyme abnormalities of glycolysis. *Blood.* 2005;106(13):4034.
23. Rijksen G, Staal GEJ. Purification and some properties of human erythrocyte hexokinase. *Biochimica et Biophysica Acta (BBA) - Enzymology.* 1976;445(2):330-341.
24. Roth EF, Jr. Malarial parasite hexokinase and hexokinase-dependent glutathione reduction in the Plasmodium falciparum-infected human erythrocyte. *J Biol Chem.* 1987;262(32):15678-15682.
25. Greenwood BM, Fidock DA, Kyle DE, Kappe SH, Alonso PL, Collins A. Malaria: progress, perils, and prospects for eradication. *J Clin Invest.* 2008;118.
26. Lelli JL, Becks LL, Dabrowska MI, Hinshaw DB. ATP converts necrosis to apoptosis in oxidant-injured endothelial cells. *Free Radical Biology and Medicine.* 1998;25(6):694-702.
27. Stocchi V Fau - Magnani M, Magnani M Fau - Canestrari F, Canestrari F Fau - Dacha M, Dacha M Fau - Fornaini G, Fornaini G. Multiple forms of human red blood cell hexokinase. Preparation, characterization, and age dependence. (0021-9258 (Print)).
28. McQueen PG, McKenzie FE, Singer BH. Age-Structured Red Blood Cell Susceptibility and the Dynamics of Malaria Infections. *Proceedings of the National Academy of Sciences of the United States of America.* 2004(24):9161.
29. Thibodeaux JJ. Modeling erythropoiesis subject to malaria infection. *Math Biosci.* 2010;225.
30. Kerlin DH, Gatton ML. Preferential invasion by Plasmodium merozoites and the self-regulation of parasite burden. *PloS one.* 2013;8(2):e57434-e57434.
31. Wagner MA, Andemariam B, Desai SA. A Two-Compartment Model of Osmotic Lysis in Plasmodium falciparum-Infected Erythrocytes. *Biophysical Journal.* 2003;84:116-123.
32. Saliba KJ, Krishna S, Kirk K. Inhibition of hexose transport and abrogation of pH homeostasis in the intraerythrocytic malaria parasite by an O-3-hexose derivative. *FEBS Letters.* 2004;570(1-3):93-96.
33. Slavic K, Krishna S, Derbyshire ET, Staines HM. Plasmodial sugar transporters as anti-malarial drug targets and comparisons with other protozoa. *Malaria Journal.* 2011;10(1):165.
34. Ortiz D, Guiguemde WA, Johnson A, et al. Identification of Selective Inhibitors of the Plasmodium falciparum Hexose Transporter PfHT by Screening Focused Libraries of Anti-Malarial Compounds. *PLOS ONE.* 2015;10(4):e0123598.

CHAPTER 5

CONCLUSIONS

The three specific research aims utilized mathematical modeling to provide novel insights into various health and disease contexts.

SPECIFIC AIM 1: We extended an existing mathematical to quantify glucose and Na reabsorption through SGLT2 in healthy, controlled, and uncontrolled diabetes and following treatment with canagliflozin. In healthy, controlled diabetic, and uncontrolled diabetic states, Na reabsorption through SGLT2 was found to be 5.7%, 11.5%, and 13.7% of total renal Na reabsorption, and 7.1% to 9.5%, 14.4% to 19.2%, and 17.1% to 22.8% of Na reabsorption in the PT alone. The model predicted that treatment of controlled diabetes with canagliflozin returns PT Na reabsorption through SGLT2 to normal levels. The degree of increased PT Na reabsorption due to SGLT2 is likely sufficient to drive pathologic changes in renal hemodynamics, and restoration of normal Na reabsorption through SGLT2 may contribute to beneficial renal effects of SGLT2 inhibition.

SPECIFIC AIM 2: We developed telemetry methods to detect and monitor physiological changes in nonhuman primates prior to and during malaria infection. Our results show, for the first time, that host physiological perturbations can be detected while malaria parasites are multiplying in the liver, a step that precedes blood-stage infections and symptomology. Early

detection of physiological changes due to infectious diseases could guide treatment prior to the onset of symptoms and pathogenic consequences. Thus, these data provide an impetus for the development of novel preemptive telemetry systems for the diagnosis of malaria and possibly other infectious diseases.

SPECIFIC AIM 3: To investigate how the malaria life cycle synchronizes with the host's glucose concentration and metabolism, we constructed a model that incorporates plasma glucose and insulin dynamics, glucose transport into red blood cells, and erythrocytic glucose conversion to ATP. By modeling diurnal glucose concentrations and incorporating parasite dynamics, we were able to reproduce erythrocytic ATP depletion indicative of RBC bursting after about 18-24 hours depending upon the parasite growth function. Night vs day meal simulations had an effect on the shape of the curves for erythrocytic ATP and glucose concentrations and parasite growth and glucose utilization. However, it had a limited effect on the time of estimated RBC bursting due to ATP depletion. This model could help inform future experiments that could be done to provide endpoints to further inform our understanding of host glucose and ATP depletion and parasite synchronization of bursting.